Next generation of grid-connected photovoltaic systems: modelling and control

Allan Fagner Cupertino[a,*], Heverton Augusto Pereira[b]

[a] *Department of Materials Engineering, Federal Center for Technological Education of Minas Gerais: Av. Amazonas, 5253, 30.421-169 Belo Horizonte - MG, Brazil.*
[b] *Department of Electrical Engineering, Federal University of Viçosa: Av. P.H. Rolfs, s/n, 36570-900, Viçosa - MG, Brazil*

Abstract

Photovoltaic (PV) systems are the most popular and spread around the world generation system. Both characteristics are due the inverter power ranges available in the market, starting with small power of tens of Watts until high-power versions. Thus, this technology can be installed in farms, small villages, cities and in large photovoltaic power plants. In the history, there has never been such type of popularity. The high-power version, in general, is composed of three-phase PV inverters and hundreds of photovoltaic panels. On the other hand, the low-power version is connected to single-phase system, with few photovoltaic panels units. When these converters are connected to the power system, referred in this Chapter as grid-connected photovoltaic systems, they need to comply with grid code standards. This chapter intends to explore some structures implemented in the PV inverter firmware, which allow the inverter connection during normal grid conditions, and how the inverter can contribute to the power system during grid voltage disturbances. Moreover, strategies to reduce the harmonic current flowing into the grid are explored. Due to the large amount of information, the authors focus their efforts to describe this problematic in single-phase inverters. This type of converter is

*Corresponding author
Email addresses: afcupertino@ieee.org (Allan Fagner Cupertino), heverton.pereira@ufv.br (Heverton Augusto Pereira)
URL: www.gesep.ufv.br (Allan Fagner Cupertino)

widespread around the power system, and with the implementation of ancillary services, they can improve the local power grid quality. Finally, it is highlighted that PV system integration is a multidisciplinary topic, where semiconductor technologies, control strategies, power system integration and grid standards need to converge in a commercial product able to perform with excellence, and also with competitive cost.

Keywords: ancillary services, advanced control functions, grid-connected photovoltaic systems, grid-friendly photovoltaic inverter, harmonic current compensation, reactive power support

1. Introduction

Solar photovoltaic (PV) industry has experienced high growth rate in the last decades. This fact can be related to the global aim to introduce renewable energy sources in the power system and the declining cost of PV panels. According to [1], a reduction in the price of grid-connected PV systems for residential applications in USA from 0.18 USD/kWh in 2016 to 0.05 USD/kWh by 2030 is recommended. This challenging reduction in price (more than 3 times) is justified by the required additional costs to facilitate grid integration and increased flexibility of PV systems.

The PV inverter converts the direct current generated by the PV panels in alternating current and injects the generated power into the grid. The PV inverter must have a high conversion efficiency and fulfill the requirements of the modern grid codes. Therefore, the inverter power must be compatible to the PV array power. Usually, the manufacturers recommend a maximum inverter sizing ratio (ISR). ISR is defined as follows:

$$ISR = \frac{p_{\mathrm{pv,p}}}{p_{\mathrm{i,r}}}, \tag{1}$$

where $p_{\mathrm{pv,p}}$ is the peak power of PV panel under standard conditions (STC)[1]

[1]The standard conditions are defined as: $G = 1000$ W/m^2 for solar irradiance; $T = 25$ °C

and $p_{\mathrm{i,r}}$ is the inverter rated power. Typical values of ISR range from 0.8 to 1.5 [2, 3]. As observed, the PV array is usually oversized to increase the energy yield. However, the injected power is limited when the generated power is higher than the inverter rated power (e.g., in summertime), which can generate energy losses. This fact is illustrated in Fig. 1a. Therefore, the optimum ISR is usually computed based on the system costs and the installation sites [4]. Independently of the adopted ISR, the PV inverter presents a margin in terms of current because the solar irradiance varies during the day. This fact is illustrated in Figure 1b, considering a typical sunny day. As observed, the operation area is about 30 % of the inverter total capacity. Therefore, the available area (≈ 70 %) may be used to provide other services to the grid [5].

In addition, the distribution system is characterized by a high penetration of nonlinear loads and PV systems. These factors lead to overall degradation of the power quality indexes. Therefore, ancillary services such as reactive power control and harmonic compensation can improve the power quality indexes and lead to grid-friendly photovoltaic systems. Therefore, the next generation of PV

for PV panel temperature and air-mass AM 1.5.

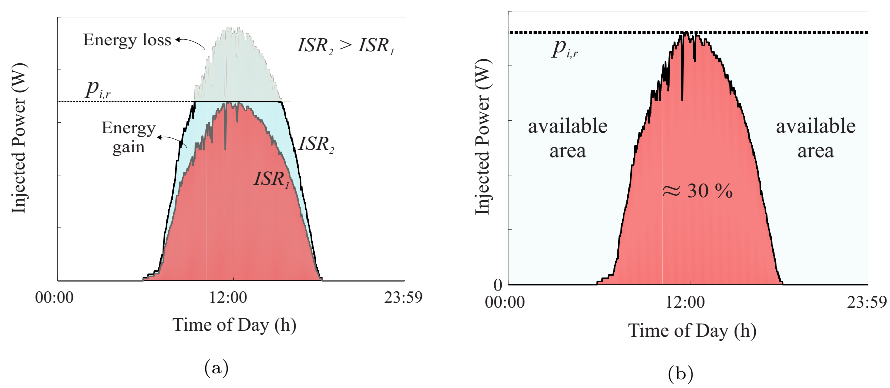

Figure 1: Operation characteristics of a PV inverter: (a) Effect of ISR in the PV inverter operation curve for a typical sunny day; (b) PV inverter operation curve for a typical sunny day and available area for ancillary services.

systems with ancillary services is expected. Under such conditions, more PV systems can be installed in a power system without requiring improvements in the grid facilities.

Due to the high variety of topologies, different control strategies for PV inverters have been proposed in the literature. In general, the control functions can be classified in three groups: Basic functions, specific functions, and advanced functions. Despite the state-of-art inverters, the next generation of PV inverters includes the ancillary functions, as illustrated in Figure 2. The also called "multifunctional PV inverter" is a breakthrough concept which has been strongly studied in recent years. Ancillary services as reactive power support, harmonic compensation and operation during unbalanced voltage conditions have been discussed and included in the PV inverter control algorithm.

Nevertheless, the next generation of PV inverters poses new challenges. Indeed, the multifunctional operation requires additional structures, which include reactive power measurement schemes, harmonic detection structures and advanced harmonic current controllers. These topics have been strongly discussed in recent years [6].

In addition, the multifunctional operation affects the inverter operation. For example, the harmonic current compensation can affect the efficiency of

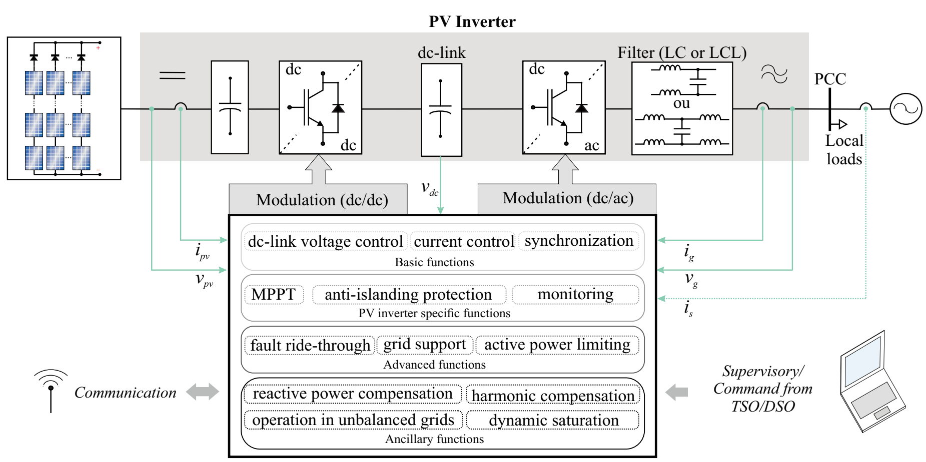

Figure 2: General control structure of the next generation of PV inverters.

maximum power point tracking, as recently discussed in [7]. Furthermore, since the solar irradiance changes during the day (as shown in Fig. 1), the current margin for reactive power control and harmonic current compensation changes during the day. Therefore, dynamic saturation schemes must be included in the control algorithm to guarantee that the inverter will operate beyond its rated current, as recently discussed in [5, 8].

This Chapter discusses the modelling and control of the next generation of PV inverters with ancillary services capability. Reactive power control and harmonic current compensation are approached. The following contributions are provided:

- Proposal of dc/dc converter control schemes to mitigate the effects of the voltage ripple in single-phase systems;
- Proposal of an improved reactive power control strategy when stationary-reference frame current control is employed;
- Benchmarking of dynamic saturation algorithms for multifunctional PV inverters with reactive power control and harmonic current compensation functions.

The obtained results are based on analytical models, simulations and experiments of a two-stage single-phase PV inverter. Moreover, this Chapter provides a comprehensive survey on the PV panel technologies, maximum power point tracker implementation, grid-connected PV systems architectures and traditional control schemes for PV inverters.

This Chapter is organized in 9 sections. Section 1 presents a brief introduction. Section 2 discusses the PV panel technologies and the mathematical modelling. Section 3 compares the main architectures of grid-connected PV systems. Section 4 discusses the implementation of the maximum power point tracker. Section 5 presents the dynamic modelling and control of dc/dc converters. Proposals to attenuate the voltage ripple in single-phase systems are presented and compared. Section 6 presents the dynamic modelling and control of the PV inverter. Section

7 is focused on the reactive power support. An improved reactive power control strategy is proposed in this section. Section 8 is focused on harmonic current compensation. Two dynamic saturation algorithms which guarantee partial harmonic compensation are experimentally compared. Finally, the conclusions are stated in Section 9.

2. PV panel modelling

2.1. PV cell technology

A PV cell is basically a p-n junction. PV cells can be made of several types of semiconductors using different manufacturing processes. When the cell is exposed to light, charge carriers are generated leading to an electric current, if the cell is connected to an external circuit. Charges are generated when the photon energy is sufficient to break the covalent bonds of the semiconductor material. This phenomenon depends on the semiconductor material and on the wavelength of the incident light [9]. The semiconductor bandgap, reflectance of the cell surface, intrinsic carrier density, the carriers mobility, the recombination rate and temperature, are factors which directly affect the characteristics of a PV cell [9, 10]. Table 1 summarizes the PV cells technologies, their market share and the maximum reached efficiencies. Three groups can be identified:

- 1st Generation - crystalline silicon cells: These cells are based on monocrystalline silicon (c-Si) or polycrystalline silicon (m-Si). These were the first PV technologies with commercial success. In 2017, the 1st generation represented about 95 % of the market [11]. c-Si cells present higher efficiencies than m-Si cells. However, the m-Si cells present lower production costs. Thereby, m-Si cells dominate the market.

- 2nd generation - Thin-film cells: These cells are based on depositing one or more thin layers on a substrate, such as glass, plastic or metal. The thickness of the film can vary from few nanometers to tens of micrometers (100 times thinner than the first generation) [9]. Different materials are

Table 1: Overview of the main PV cells technology. The annual production for 2017 were obtained from [11]. The efficiency data were obtained from the NREL chart [12].

	Generation	Technology	Production (2017)	Maximum Efficiency (2020)
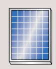	Crystalline silicon	c-Si	32.2 GWp	26.7 %
		m-Si	60.8 GWp	23.3 %
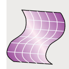	Thin-Film	a-Si	0.3 GWp	14.0 %
		CIGS	1.9 GWp	23.4 %
		CdTe	2.3 GWp	22.1 %
		GaAs	-	29.1 %
	Advanced new concepts	MPV*	-	47.1%
		OPV	-	17.4 %
		DSSC	-	12.3 %
		Hybrid**	-	25.2 %

*The efficiency corresponds to a 6 junction cell with concentrator.

** The efficiency data for hybrid technology corresponds to a perovskite-based solar cell.

employed as amorphous silicon (a-Si), copper indium gallium diselenide (CIGS) and cadmium telluride (CdTe). In 2017, the 2nd generation corresponded to 5 % of the market [11]. This technology lead to lighter and flexible cells. Thin-film cells are cheaper than silicon cells, however, the second generation is generally less efficient. In recent years, several improvements have been implemented to improve the efficiency of this type of cell. An exception is the PV cell based on gallium arsenide (GaAs), which are more efficient than the 1st generation. However, the production costs of GaAs solar cells are still high.

- 3rd generation - Advanced cells: This generation is based on modern materials. The multijunction solar cells (MPV), organic PV cells (OPV) and the dye-sensitized solar cells (DSSC) are included in this group. The concentrated solar cells (CPV) is also an approach to improve the cell efficiency. Most of these technologies are under research and development stage. A promising member of this group is the perovskite-based solar cell. In 2020, this technology exceeded the maximum efficiency achieved by m-Si PV cells and presents low production costs [12]. The major drawback of the 3rd generation cells is the stability, a challenge addressed in recent research.

2.2. PV panel Mathematical Model

Typical commercial PV panels are build with 60, 72 or 96 (recently) series-connected cells. The electric characteristics of a PV panel are summarized in Fig. 3. The following conclusions can be stated:

- The PV panel presents a nonlinear behavior (current source behavior for low voltages and voltage source behavior for higher voltages) as shown in Fig. 3a. In addition, the PV panel I-V curve presents 3 remarkable points: the short-circuit point $(0, i_{\mathrm{sc}})$, the open-circuit voltage $(v_{\mathrm{oc}}, 0)$ and the maximum power point $(v_{\mathrm{mp}}, i_{\mathrm{mp}})$;
- The short-circuit current i_{sc} is more sensitive to the solar irradiance G than the PV panel temperature T. On the other hand, the open-circuit voltage v_{oc} is more sensitive to the PV panel temperature T than the solar irradiance G. These facts lead to the P-V curve behavior illustrated in Figures 3b and 3c;
- The increase of the PV panel temperature or decrease in solar irradiance decreases the generated power, as shown in Figure 3c;
- The PV panel presents a maximum power which is a function of the climatic conditions. Therefore, a maximum power point tracker (MPPT) must be implemented in the PV inverter control algorithm.

Different mathematical models were developed to approximate the electrical behavior of PV panels with different levels of detail and complexity [13]. The single-diode model is presented in Figure 3d. In this model, the PV cell is modeled by a current source in parallel with a diode. The series and parallel

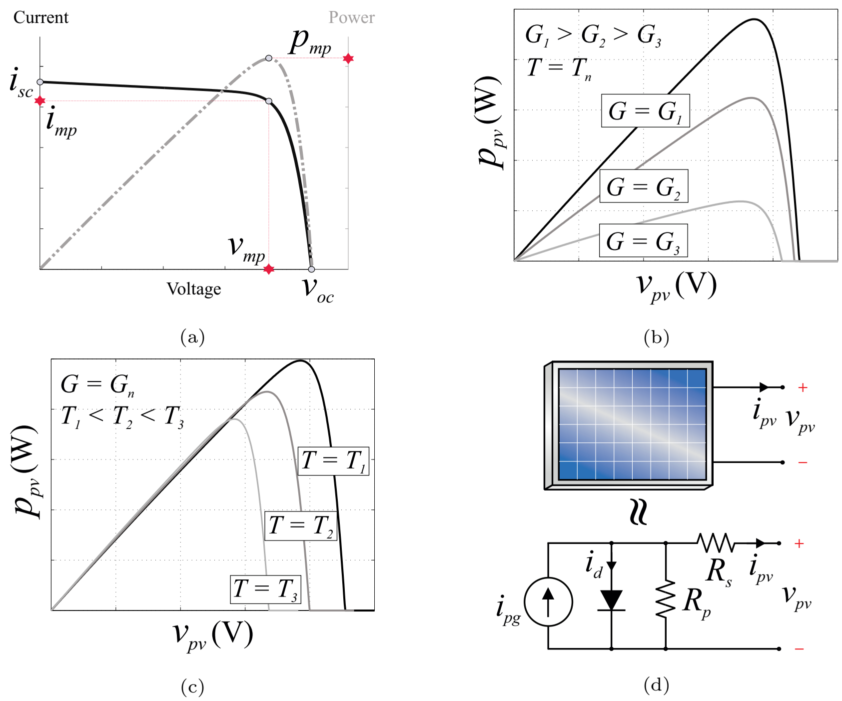

Figure 3: Electric characteristics of a PV panel: (a) Generic I-V and P-V curves; (b) Effect of the solar irradiance in the P-V curves; (c) Effect of the cell temperature in the P-V curves; (d) Single-diode model.

resistances R_s and R_p represent the voltage drop when charges migrate from the electrical contacts and the reverse leakage current of the diode, respectively.

Other approach is the two-diode model. This second diode represents the recombination carriers in the pn junction [13]. Moreover, according to [14], the series resistance R_s decreases with the voltage while the parallel resistance R_p decreases with the temperature. However, these models usually require experimental characterization of the PV panel. On the other hand, the single-diode model parameters can be obtained based on the datasheet parameters, as proposed by [15, 16]. Therefore, the single-diode model can be considered a trade-off of precision and complexity [16].

In the single-diode model, the I-V curve is expressed by:

$$i_{\mathrm{pv}} = i_{\mathrm{pg}} - \underbrace{i_0 \left[\exp\left(\frac{v_{\mathrm{pv}} + R_{\mathrm{s}} i_{\mathrm{pv}}}{a v_{\mathrm{t}}}\right) - 1\right]}_{i_{\mathrm{d}}} - \frac{v_{\mathrm{pv}} + R_{\mathrm{s}} i_{\mathrm{pv}}}{R_{\mathrm{p}}}, \tag{2}$$

where i_{pg} is the photoelectric current and i_0 is the diode reverse saturation current. a is the diode ideality constant, typically in the range $1 \leq a \leq 1.5$, where $a = 1$ means an ideal diode. v_{t} is the PV module thermal voltage, given by:

$$v_{\mathrm{t}} = \frac{N_{\mathrm{s}} k T}{q}, \tag{3}$$

where N_{s} is the number of series connected cells, k is the Boltzmann constant ($1.3806\ 10^{-23}$ J/K), T (K) is the cell temperature and q is the electron charge ($1.602\ 10^{-19}$ C).

The current i_{pv} is proportional to the solar irradiance and varies linearly with the cell temperature. Accordingly:

$$i_{\mathrm{pg}} = (i_{\mathrm{pg_n}} + K_{\mathrm{i}} \Delta T) \frac{G}{G_{\mathrm{n}}}, \tag{4}$$

where $\Delta T = T - T_{\mathrm{n}}$ and K_{i} (A/K) short-circuit current temperature coefficient. $i_{\mathrm{pg_n}}$ is the photoelectric current at standard conditions ($G_{\mathrm{n}} = 1000$ W/m^2 and $T_{\mathrm{n}} = 25$ °C), computed as follows:

$$i_{\mathrm{pg_n}} = i_{\mathrm{sc_n}} \left(\frac{R_{\mathrm{p}} + R_{\mathrm{s}}}{R_{\mathrm{p}}}\right), \tag{5}$$

where $i_{\mathrm{sc_n}}$ is the short-circuit current at standard conditions.

On the other hand, the reverse saturation current can be estimated by [16]:

$$i_0 = \frac{i_{\mathrm{sc_n}} + K_{\mathrm{i}} \Delta T}{\exp\left(\frac{v_{\mathrm{oc_n}} + K_{\mathrm{v}} \Delta T}{a v_{\mathrm{t}}}\right) - 1}, \tag{6}$$

where $v_{\mathrm{oc_n}}$ is the open-circuit voltage at standard conditions. K_{v} is the open-circuit voltage temperature coefficient.

It is important to remark that the series and parallel resistances and the diode ideality factor are not provided in the datasheets. Indeed, the series and parallel resistance affect the remarkable curves of Figure 3a. On the other hand, the ideality factor affects the curvature of the I–V curve. Therefore, references [15, 16] proposed algorithms to estimate R_s and R_p requiring only the I-V curve remarkable points. Then, additional points can be used to estimate the ideality factor [13].

Table 2 compares the data provided in the datasheet of JKM260P-60B PV panel manufactured by Jinko Solar and the obtained results for the algorithm proposed by [16]. The algorithm is available for download in [17]. The simulated I-V and P-V curves are presented in Figures 4a and 4b. As observed, this model can represent the electric characteristics of the PV panel with a negligible error for high irradiance values.

Table 2: Comparison of the parameters provided by the manufacturer and the results of the modelling algorithm.

Parameters	Datasheet*	Model
$v_{\mathrm{oc_n}}$	38.1 V	38.1 V
$i_{\mathrm{sc_n}}$	8.98 A	8.98 A
v_{mp}	31.1 V	31.1 V
i_{mp}	8.37 A	8.37 A
p_{mp}	260.31 W	260.31 W
K_i	0.0054 A/K	-
K_v	-0.1181 V/K	-
R_s	-	0.277 Ω
R_p	-	162.92 Ω
a	-	1

*Standard Conditions: $G = 1000$ W/m^2 and $T = 25$ °C.

Finally, it is important to remark that the solar irradiance and the PV panel temperature are correlated. Indeed, the higher the irradiance, the higher the PV panel temperature. Usually, the manufacturers also provide the PV panel electrical characteristics at the nominal operating cell temperature ($NOTC$).

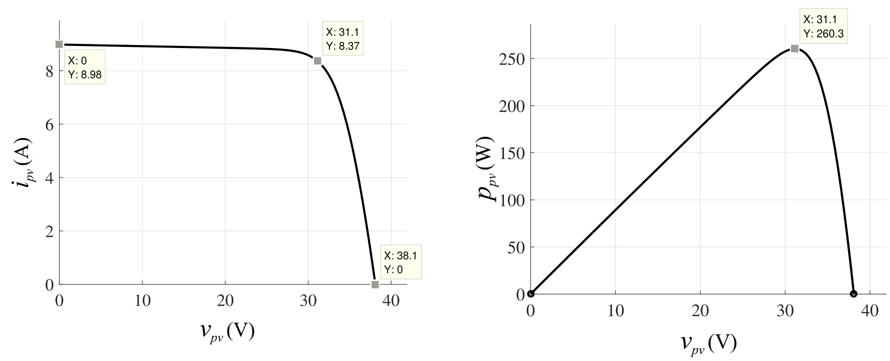

(a) (b)

Figure 4: Simulated electric characteristics of the PV panel JKM260P-60B: (a) I-V curve; (b) P-V curve.

The $NOTC$ is measured for $G = 800$ W/m^2, ambient temperature $T_\mathrm{a} = 20$ °C and wind speed of 1 m/s. Different models for the PV panel thermal dynamics have been discussed in literature [18]. Nevertheless, the steady-state temperature is enough to evaluate the performance of the PV inverter. The steady-state PV panel temperature can be roughly estimated by the following linear equation:

$$T = T_\mathrm{a} + (NOTC - 20)\,\frac{G}{800}. \tag{7}$$

2.3. PV panel linearization

The electric characteristics of the PV panel are nonlinear. This fact makes difficult the dynamic modelling of the MPPT. A possible solution to this problem is to obtain a linear approximation of the PV panel characteristic around the maximum power point, i.e., a small-signal model. It is important to remark that the quiescent point chosen is the maximum power point, since it is the desirable steady-state condition.

Figure 5a presents the idea behind the linearization. Basically, the PV panel curve is approximated by a Thévenin equivalent circuit (TEC) with voltage v_th and resistance R_th. These parameters can be computed as follows:

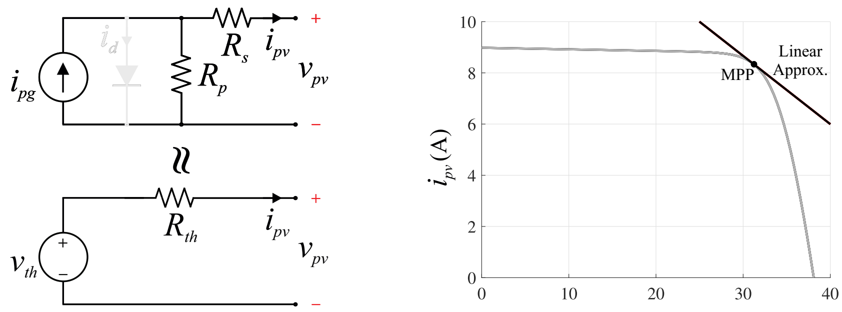

(a) (b)

Figure 5: Small-signal model of the PV panel: (a) Simplification of the equivalent circuit model; (b) Comparison of the I-V curve obtained from the mathematical model and TEC. Conditions: $G = 1000$ W/m^2 and $T = 25$ °C.

$$v_{\mathrm{th}} = 2v_{\mathrm{mpp}}, \tag{8}$$

$$R_{\mathrm{th}} = \frac{v_{\mathrm{mpp}}}{i_{\mathrm{mpp}}}. \tag{9}$$

The following conclusions can be stated:

- The equations (8) and (9) guarantee that the maximum power point of TEC is identical to the mathematical model (same equivalent resistance);
- v_{th} is more sensitive to the cell temperature than the solar irradiance;
- R_{th} is more sensitive to the solar irradiance than the cell temperature;
- The I-V curve of TEC is linear while the P-V curve is quadratic. Therefore, the TEC approximation is only valid in the vicinities of the maximum power point.

The I-V curve of TEC is presented in Figure 5b. This model will be employed in next sections to model the MPPT and in the control tuning.

3. PV System Architectures

Figure 6 presents an overview of different architectures of PV systems. The products available in the market can be single-stage or two-stage inverters (including a dc/dc converter). The architectures can be classified according to the inverter concept, as follows:

- Microinverter: In this approach, one inverter is connected to 1 or 2 solar panels. This solution minimizes the energy losses associated to the PV panels mismatch and shadows. Furthermore, the dc wiring length is minimized. The main drawback is the inverter cost and efficiency. Since power density is important in microinverters, high switching frequencies are employed and their power stage is based on MOSFETs;

- String inverters: This approach connects the inverter in a string of panels. Therefore, the MMPT is not performed individually, resulting in higher energy losses due to mismatch and shadows. Most of string inverters are based on IGBTs because they are cheaper than MOSFETs for the same current and voltage ratings. Many products in the market are based on 2 stage topologies, since the dc/dc stage increases the input voltage range of the equipment;

- Power optimizers: Similarly to the microinverter concept, the power optimizer is connected to a single PV panel. Power optimizers are dc/dc converters with low voltage gain, are based on MOSFETs and present high efficiency ($\leq 98.5\%$). The power optimizers are cascaded-connected, and the resultant string is connected to a string inverter. As advantages, the power optimizer presents flexibility regarding the inverter firmware update (a single string inverter is employed despite the microinverter approach). The power optimizer also increases the safety, since the PV module voltage is reduced to very low values when the inverter stage is not operating (e.g. open-circuit voltage condition);

- Multi-string inverters: This approach is an extension of string inverters. The topology presents more than one dc/dc stage. Under such conditions, the MPPT is performed per string. This topology is also interesting in rooftop PV systems where the roof presents different orientations. Most of products are based on IGBTs.

- Central inverters: This approach is used in solar power plants. Single-stage inverters based on IGBTs are usually employed, which leads to higher efficiency and lower cost per kW than string inverters. Many independent inverters are employed in multi-megawatt plants to increase the reliability. Strings of 1 or 1.5 kV volts are employed, which leads to higher losses due to shadows and PV panels mismatch.

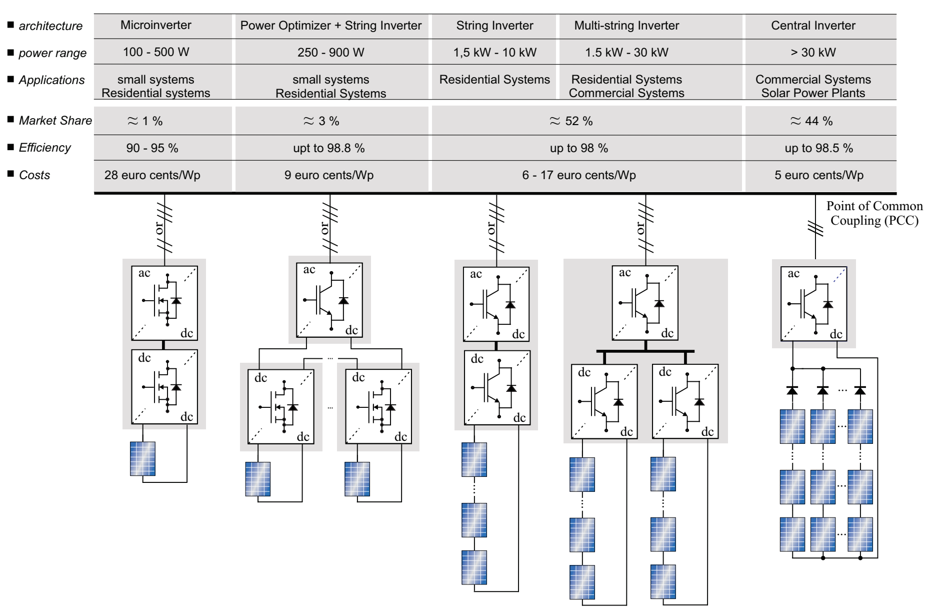

Figure 6: Overview of the main PV system architectures. The data of market share, efficiency and estimated costs corresponds to 2017 [11].

Furthermore, the PV inverters can be classified according to the galvanic isolation, which is very important to reduce the leakage currents[2]. According to the Figure 7. Three groups are identified:

- Inverter with line frequency transformer: This topology is presented in Fig. 7a. The line frequency transformer minimizes the leakage currents and provide galvanic isolation. Additionally, the transformer turns ratio increases the inverter design flexibility. However, this approach increases the weight, the volume and the losses of the PV system;

- Transformerless inverters: In this case, the inverter does not present any galvanic isolation, as shown in Fig. 7b. This approach leads to higher efficiency. However, a careful topology selection and filter design must be accomplished to minimize the leakage currents[3];

- Inverters with high frequency transformer: This topology is presented in Fig. 7c. This approach employs a galvanic isolated dc/dc converter. The transformer is designed to operate at high frequencies (kHz range) reducing considerably the volume and weight. The transformer also improves the inverter input voltage range. However, the transformer is an additional stage, which affects the inverter efficiency. Furthermore, the complexity of the dc/dc stage increases, which leads to reliability concerns and higher costs.

The line frequency transformer approach is widely used in central inverters since the PV power plants are usually connected to the medium or high voltage systems. When only the frame of the PV panel is grounded, the transformerless inverters are preferred. Therefore, transformerless inverters are widely employed in residential and commercial systems. It is important to remark that when

[2]The leakage current flows through the PV panels parasitic capacitance and is related to the common mode voltage generated by the inverter modulation.

[3]Reference [19] presents a comprehensive review of recent topologies for transformerless PV inverters.

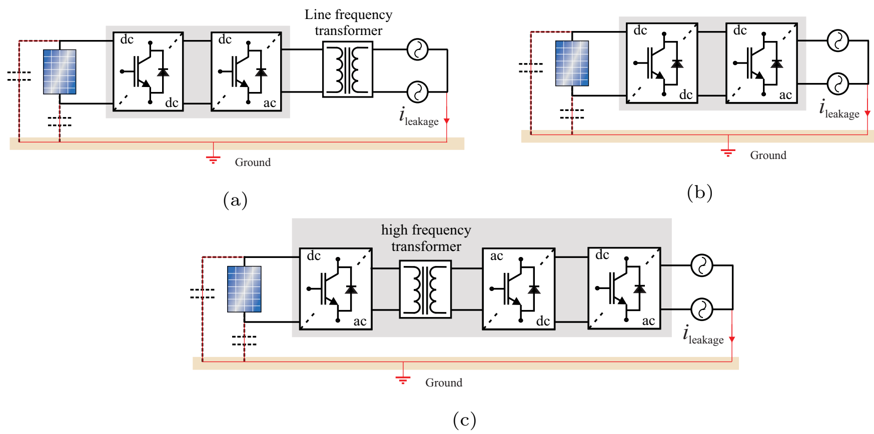

Figure 7: Classification of PV inverters in terms of galvanic isolation: (a) PV inverter with line frequency transformer; (b) Transformerless PV inverter; (c) PV inverter with high frequency transformer.

thin-film modules are taking into account, the grounding of positive (or negative) terminal of the PV array is recommended [20]. Under such conditions, the use of inverters with galvanic isolation is indispensable.

Figures 8a and 8b present the schematic of a two-stage PV transformerless inverter for single and three-phase system, respectively. These topologies are based on dc/dc boost converter and full-bridge inverter. Several commercial PV inverters employ topologies inspired in this basic approach. Therefore, this chapter focus on this topology. The single-phase inverters are considered because they are employed in several residential and commercial systems. The modelling and control of the single-phase topology is approached in the next sections. It is important to remark those concepts presented in this chapter can be extended to other PV inverter topologies.

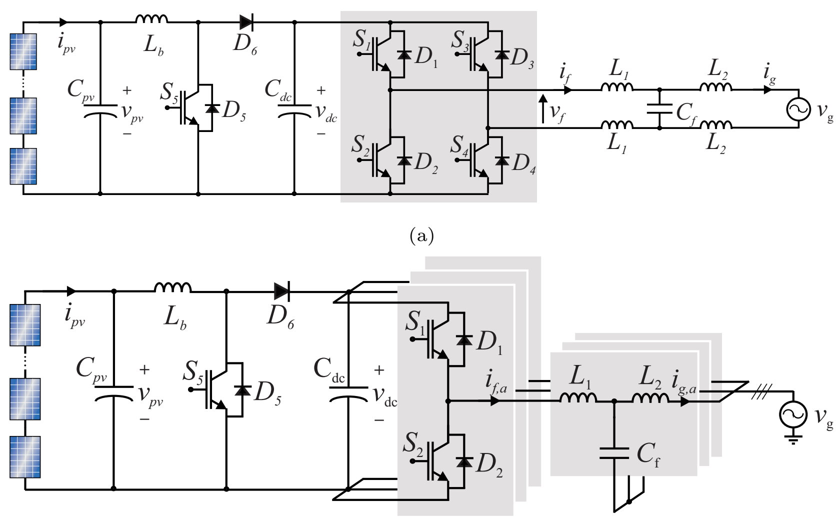

(a)

(b)

Figure 8: Example of transformerless inverter based on boost converter and full bridge inverter: (a) Single-phase; (b) Three-phase.

4. Maximum power point tracking - MPPT

4.1. Fundamentals

The MPPT guarantees the maximum power transfer from the PV panels to the grid, through a power converter. The control scheme includes a MPPT algorithm. This iterative algorithm measures the PV array voltage and/or current and provides a reference to the control scheme. Then, the power converter is responsible to impose this reference at the solar panel terminals. Figure 9a presents the current-based MPPT. In this case, the MPPT algorithm computes the maximum power point current and a current-source converter is employed. On the other hand, Figure 9b presents the voltage-based MPPT. In this case, the MPPT algorithm computes the maximum power point voltage and a voltage-source converter is employed.

Tens of MPPT algorithms have been proposed in literature [21]. The most popular are based on the hill climbing approach, as illustrated in Figures 9c and 9d. The reference voltage (or current) is incremented and the behavior of the output power is observed. If the output power increases, the reference is incremented in the same direction. Otherwise, the reference is incremented in the opposite direction. Therefore, the PV inverter response will oscillate around the maximum power point. As observed in Figures 9c and 9d, the derivative of P-I curve is higher than the derivative of the P-V curve in the right side of the maximum power point. This means that small increments in the reference current may lead to high increments in the PV array power. Therefore, voltage-based MPPTs usually lead to better steady-state response.

The performance of MPPT algorithms are affected by two parameters: the sampling frequency f_{mppt} and the voltage increment Δ_{v}. The higher the f_{mppt}, the higher the bandwidth required for the power stage. On the other hand, Δ_{v} affects both speed and accuracy of the MPPT. Therefore, some references in literature propose MPPT algorithms with variable voltage increment [21]. Recently, it was found that the MPPT algorithm parameters can also affect the inverter power quality. For more details, see [22].

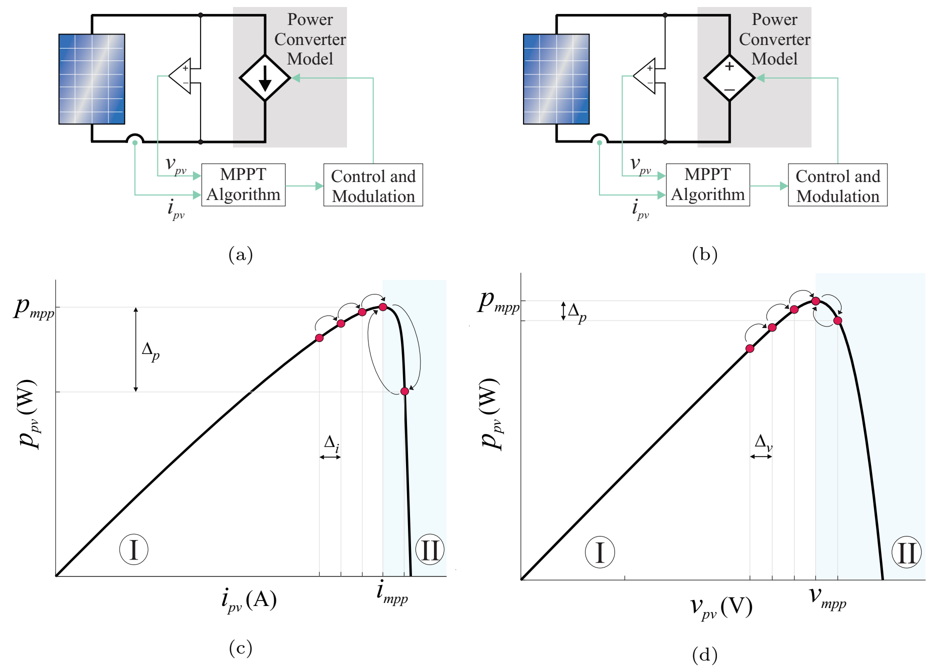

Figure 9: Maximum power point tracking fundamentals: (a) Current-based MPPT; (b) Voltage-based MPPT; (c) Basic operation of MPPT algorithm for current-based approach; (c) Basic operation of MPPT for voltage-based approach.

Typical values of f_{mppt} are in the range of 1 to 10 Hz. According to [23], a tradeoff value for the voltage increment is given by:

$$\frac{1}{1000} v_{\mathrm{mpp}} f_{\mathrm{mppt}} \leq \Delta_{\mathrm{v}} \leq \frac{1}{100} v_{\mathrm{mpp}} f_{\mathrm{mppt}}. \tag{10}$$

In addition, partial shading conditions have important effects in the MPPT performance. The partial shading can be caused by obstructions (roof top structures, buildings, trees) or deposition of snow, leaves or dust on the PV panel surface. This is illustrated in Fig. 10a. In view of this problem, diodes are integrated in the PV panel to bypass the shaded cells (usually, one diode is installed each 18 - 24 cells). The conduction of bypass diodes leads to anomalous P-V curves, as shown in Figure 10b. As observed, the P-V curve presents local maximums. Therefore, the conventional hill climbing approach can lead to the operation in a local maximum, i.e., loss of energy. Therefore, GMPPT (global maximum power point tracker) have been proposed in literature to solve this issue [21]. This is still an important research topic in PV systems.

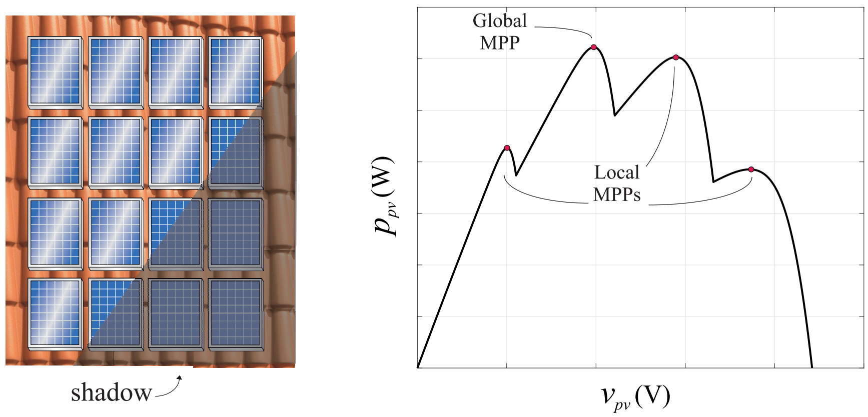

(a) (b)

Figure 10: Partial shading versus MPPT: (a) Illustration of a partial shading condition; (b) Effect of the partial shading in the P-V curve.

4.2. Architectures

In practical applications, the controlled sources in Figures 9a and 9b are replaced by a power conversion circuit. In two-stage PV inverters, the MPPT is performed by the dc/dc converter. Figure 11a and 11b present two typical measurement schemes when the boost converter is employed. As observed, the dc/ac stage of Fig. 8 is represented by a voltage source. Either PV array or the inductor current can be measured[4]. Moving average filters (MAV) are usually employed in the voltage and current measurements to remove the high frequency and low-frequency ripples. The high frequency ripple is generated by the converter switching. The low-frequency ripple (usually double-line frequency) is generated by single-phase power injection or unbalanced conditions in three-phase inverters.

[4]In steady-state, the dc component of these two currents is the same.

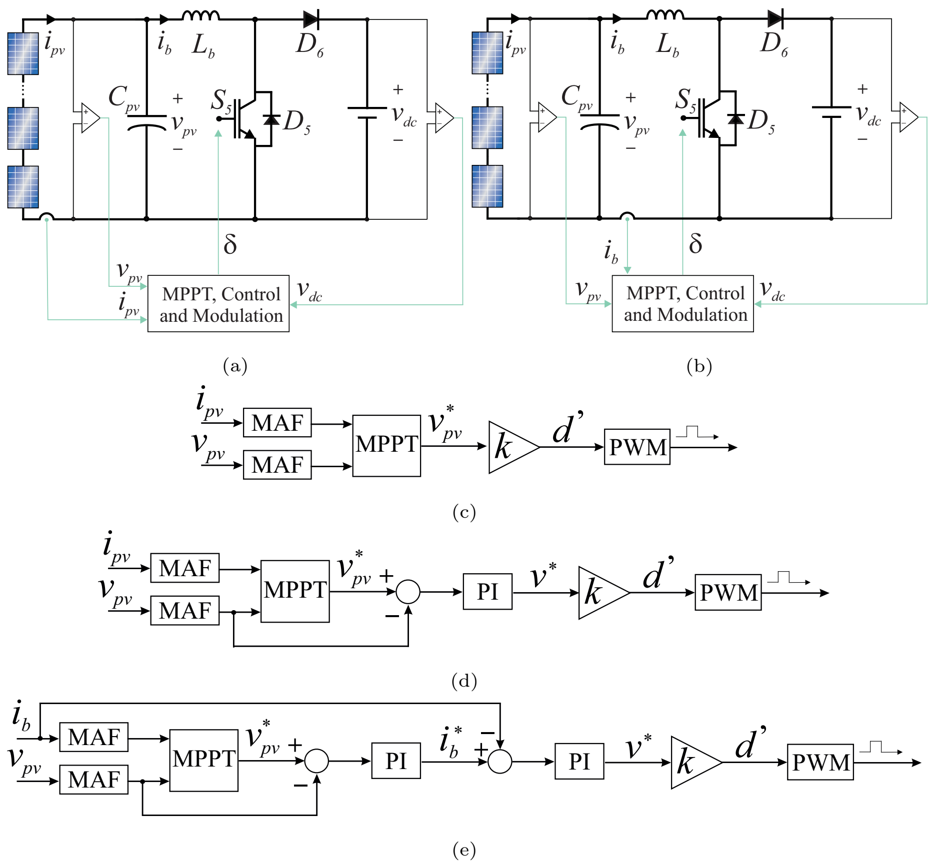

Figure 11: Architectures of the MPPT: (a) Measurement scheme 1; (b) Measurement scheme 2; (c) Open-loop voltage control; (d) Single-loop voltage control; (e) Double-loop voltage control.

Three possible control strategies are shown in Figure 11. Figure 11c presents the open-loop control strategy. The MPPT algorithm computes the maximum power point voltage v^*_{pv}. Then, the boost converter duty-cycle is computed through the following equation:

$$d = 1 - d' = 1 - kv^*_{\mathrm{pv}}, \tag{11}$$

where $k = 1/v^*_{\mathrm{dc}}$ is the normalization gain. In this technique, the voltage transient is dictated by the converter open-loop response. Since the ideal equation of the boost converter is employed, the circuit losses will lead to a steady-state error. This error is not a big issue, since the MPPT algorithm can correct the voltage reference to guarantee the operation around the maximum power point. Furthermore, this strategy can be applied for both measurement schemes shown in Figure 11a and 11b

On the other hand, Figure 11d presents the single-loop voltage control. In this case, the measured voltage is controlled by a compensator (e.g., integral, or proportional integral) and the steady-state voltage error is eliminated. Moreover, the voltage transient can be adjusted based on the compensator parameters. This approach is commonly used with the measurement scheme shown in Figure 11a

Finally, when the measurement scheme of Figure 11a is employed, the double-loop voltage control can be implemented. In this case, the outer loop controls the voltage while the inner loop controls the inductor current. It is important to remark that the inductor current loop must be faster to guarantee the stability of the closed loop system. Although this strategy increases the complexity of the control tuning (two compensators are employed), it allows to control the current transient, which might bring benefits to the semiconductor devices protection.

5. Dc/dc stage control

5.1. Dynamic modelling

The dynamic modelling of the dc/dc stage is based on the converter average model presented in Figure 12. The solar array is linearized around the maximum power point, as described in Section 2.3. The equivalent series resistance (ESR) of the capacitor C_{pv} and inductor L_{b} are considered in the modelling. Moreover, the dc-link voltage is assumed to be constant, i.e., $v_{\mathrm{dc}} = v^*_{\mathrm{dc}}$. Under such conditions, the dynamics of the boost converter can be described by the following equations:

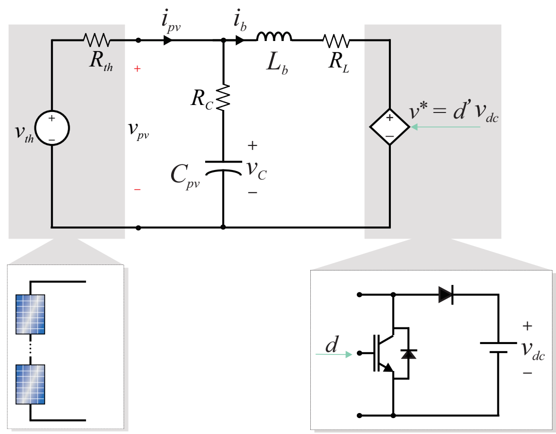

Figure 12: Average model of the dc/dc boost converter.

$$\begin{cases} \frac{v_{\mathrm{th}}-v_{\mathrm{pv}}}{R_{\mathrm{th}}} - C_{\mathrm{pv}}\frac{dv_{\mathrm{pv}}}{dt} = i_{\mathrm{b}}, \\ v_{\mathrm{pv}} - R_{\mathrm{L}} i_{\mathrm{b}} - L_{\mathrm{b}}\frac{di_{\mathrm{b}}}{dt} = d' v^{*}_{\mathrm{dc}}, \\ v_{\mathrm{pv}} = R_{\mathrm{C}}\frac{dv_{\mathrm{C}}}{dt} + v_{\mathrm{C}}. \end{cases} \tag{12}$$

where L_{b} is the inductance of boost converter, C_{pv} is the input capacitance, R_{L} is the inductor equivalent series resistance, R_{C} is the capacitor equivalent series resistance, R_{th} and v_{th} are the parameters of the linearized PV panel model, v_{dc} is the dc-link voltage and $d' = 1 - d$, where d is the converter duty-cycle. $v = d' v_{\mathrm{dc}}$ is the equivalent voltage generated by the converter switching. The dc/dc converter is controlled by the duty-cycle d, which is the ratio between the conduction time of the IGBT and the switching period, as follows:

$$d = \frac{t_{\mathrm{on}}}{T_{\mathrm{sw}}} = t_{\mathrm{on}} f_{\mathrm{sw}}. \tag{13}$$

where f_{sw} is the switching frequency.

Using these dynamic equations and applying the Laplace transform, the following transfer functions can be obtained[5]:

[5]Transfer functions are computed considering a single input and single output. For the analyzed dynamic equations, the inputs are the voltage v_{th} and the duty-cycle dependent term $v = d' v_{\mathrm{dc}}$. The terms depending on v_{th} are neglected because v_{th} is other input.

$$\frac{V_{\rm pv}(s)}{D(s)} = v_{\rm dc}^{*} \overbrace{\frac{R_{\rm C}C_{\rm pv}s + 1}{\left(LC + \frac{L_{\rm b}C_{\rm pv}R_{\rm C}}{R_{\rm th}}\right)s^2 + (R_{\rm C}C_{\rm pv} + \frac{R_{\rm L}R_{\rm C}}{R_{\rm th}}C_{\rm pv} + \frac{L_{\rm b}}{R_{\rm th}} + R_{\rm L}C_{\rm pv})s + \frac{R_{\rm L}}{R_{\rm th}} + 1}}^{G_{\rm vd}(s)}, \tag{14}$$

$$\frac{I_b(s)}{D(s)} = v_{\rm dc}^{*} \overbrace{\frac{\left(C_{\rm pv} + \frac{R_{\rm C}C_{\rm pv}}{R_{\rm th}}\right)s + \frac{1}{R_{\rm th}}}{\left(LC + \frac{L_{\rm b}C_{\rm pv}R_{\rm C}}{R_{\rm th}}\right)s^2 + (R_{\rm C}C_{\rm pv} + \frac{R_{\rm L}R_{\rm C}}{R_{\rm th}}C_{\rm pv} + \frac{L_{\rm b}}{R_{\rm th}} + R_{\rm L}C_{\rm pv})s + \frac{R_{\rm L}}{R_{\rm th}} + 1}}^{G_{\rm id}(s)}, \tag{15}$$

$$G_{vi}(s) = \frac{V_{\rm pv}(s)}{I_{\rm b}(s)} = \frac{R_{\rm C}C_{\rm pv}s + 1}{\left(C_{\rm pv} + \frac{R_{\rm C}C_{\rm pv}}{R_{\rm th}}\right)s + \frac{1}{R_{\rm th}}}. \tag{16}$$

Simulations were implemented to validate the obtained transfer functions models. A PV array with 8 series-connected JKM260P-60B PV panels is considered. Under such conditions, the Thévenin parameters can be estimated by multiplying the relations (8) and (9) by $N_{\rm ps} = 8$. The parameters of the boost converter system are shown in Table 3. These parameters were obtained from a commercial PV inverter.

Initially, the open-loop response of the converter is evaluated. The transfer function model $G_{\rm vd}$ is compared with a simulation model, which considers the

Table 3: Parameters of the boost converter considered in the simulations.

Parameters	Value
Input capacitance $C_{\rm pv}$	180 μF
Inductance $L_{\rm b}$	980 μH
Inductor ESR $R_{\rm L}$	40 mΩ
Capacitor ESR $R_{\rm C}$	300 mΩ
Dc-link voltage reference $v_{\rm dc}^{*}$	360 V
Switching frequency $f_{\rm sw}$	20,040 Hz
Sampling frequency $f_{\rm s}$	20,040 Hz

single-diode model for the PV array and the converter modulation and switching process. The transfer function G_{vd} is computed considering the R_{th} for $G = 1000$ W/m^2 and $T = 25$ °C. The tests are conducted in two different conditions to evaluate the robustness of the proposed model. The converter duty-cycle in steady-state for operation in the maximum power point can be roughly estimated by:

$$d = \frac{v_{\mathrm{dc}}^{*} - v_{\mathrm{mp}}}{v_{\mathrm{dc}}^{*}}. \tag{17}$$

For the considered PV panel, $d \approx 0.31$ at STC. Disturbances around the steady-state value are applied. The results obtained for STC are presented in Figure 13a. As observed, the model represents the average dynamics of the PV panel voltage. Both damping and natural frequency are well represented for voltage values higher and lower than v_{mpp}. On the other hand, Figure 13b presents the results for $G = 600$ W/m^2 and $T = 42.25$ °C. This temperature was computed based on equation (7). As observed, the damping observed in the complete system is higher. This is observed because the real value of R_{th} for the considered operation conditions is higher than the value obtained at STC. The results of Figures 13a and 13b also indicate that the boost converter open-loop response is stable but presents a quite reduced damping. This response can be improved by closed loop strategies.

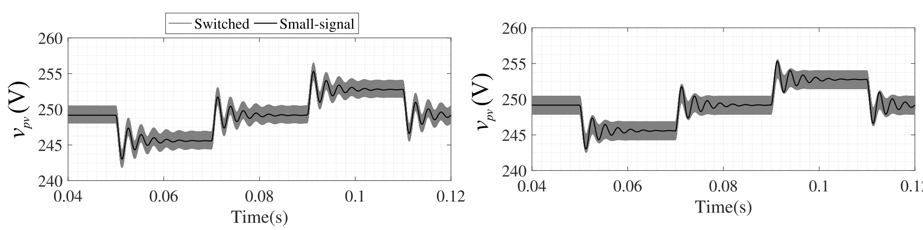

(a) (b)

Figure 13: PV panel voltage dynamic response as a function of disturbances in the converter duty-cycle (a) $G = 1000$ W/m^2 and $T = 25$ °C; (b) $G = 600$ W/m^2 and $T = 42.25$ °C. The initial value of duty-cycle is approximately 0.31 and the employed disturbance is ± 0.01.

5.2. Control tuning

This section describes the control tuning and evaluate the response of the different MPPT architectures illustrated in Figure 11. Figure 11c presented the open-loop scheme. In this approach, no compensator is employed, and the dynamic response is dictated by the step response of the function G_{vd}.

On the other hand, the complete block diagram for the single-loop control strategy is presented in Figure 14. This block diagram includes two additional transfer functions. $G_{\mathrm{d}}(s)$ represents the model of the PWM modulator and the delay caused by the digital implementation of the controller. Usually, the PWM modulator is modelled by a zero-order hold function. Assuming the control sampling frequency equal to the switching frequency, one sample delay is obtained in the digital implementation [24]. Accordingly, the transfer function G_{d} is modeled as follows:

$$G_{\mathrm{d}}(s) = \frac{1 - e^{-T_{\mathrm{sw}}}}{T_{\mathrm{sw}} s} e^{-T_{\mathrm{sw}}} \approx \frac{1}{1.5 T_{\mathrm{sw}} s + 1}. \tag{18}$$

where the usual approximation for a first-order system with time constant $\tau = 1.5T_{\mathrm{sw}}$ is employed to simplify the control tuning.

As previously mentioned, the voltage v_{pv} presents low and high-frequency ripple. Therefore, some filtering must be employed in this technique. A moving average filter (MAV) is employed here. The moving average window N can be computed by:

$$N = \frac{f_{\mathrm{sw}}}{f_{\mathrm{m}}} \tag{19}$$

where f_{m} is usually adopted as the second harmonic of the line frequency, i.e., $f_{\mathrm{m}} = 120$ Hz [6]. Under such conditions, both low and high-frequency harmonics are attenuated. The dynamics of a moving average filter can be approximated by the following equation:

[6] In this Chapter, 60 Hz systems are considered.

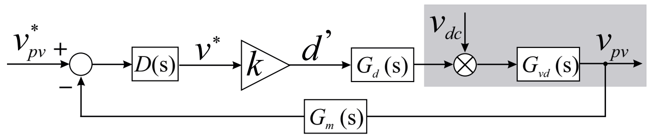

Figure 14: Block diagram of the single-loop control scheme. In this subsection, $v_{\mathrm{dc}} = v_{\mathrm{dc}}^*$ is assumed, i.e. $kv_{\mathrm{dc}} = 1$

$$G_{\mathrm{m}}(s) \approx \frac{1}{0.25T_{\mathrm{m}}s + 1}. \tag{20}$$

where $T_{\mathrm{m}} = \frac{1}{f_{\mathrm{m}}}$.

Under such conditions, assuming that $v_{\mathrm{dc}} = v_{\mathrm{dc}}^*$, the normalization factor $k = \frac{1}{v_{\mathrm{dc}}^*}$ cancels out the plant multiplication term. Therefore, the open-loop transfer function for single-loop control scheme is given by:

$$G(s) = D(s)G_{\mathrm{d}}(s)G_{\mathrm{vd}}(s)G_{\mathrm{m}}(s), \tag{21}$$

where $D(s)$ is the compensator transfer function. Usually, proportional-integral controllers are employed. Accordingly:

$$D(s) = k_{\mathrm{p,v}} + \frac{k_{\mathrm{i,v}}}{s}, \tag{22}$$

where $k_{\mathrm{p,v}}$ is the proportional gain and $k_{\mathrm{i,v}}$ is the integral gain.

Figure 15 presents the Bode diagrams of the open-loop transfer function for the uncompensated ($D(s) = 1$) and compensated transfer functions. Because of the moving average filter, the bandwidth of the compensated system is assumed to be approximately 12 Hz (one decade below the moving average filter frequency). This bandwidth also guarantees a response time *lower* than the sampling time of the MPPT algorithms (typically between 0.1 to 1 second). The compensator is designed to improve both gain and phase margin of the uncompensated system. Since the system bandwidth is around to the desired value, a simple integral controller is employed to guarantee no steady-state error. The obtained phase margin is around 69 degrees. The compensator parameters are presented in Table 4.

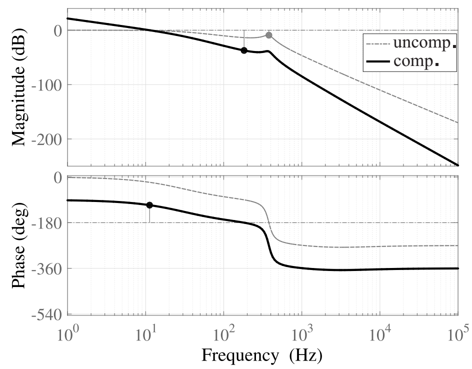

Figure 15: Bode diagram of the open-loop transfer function for both uncompensated and compensated system.

Table 4: Tuned compensator parameters.

Parameters	Single-loop control	Double-loop control
Moving average filter frequency f_m	120 Hz	120 Hz
Sampling frequency $f_\mathrm{s} = f_\mathrm{sw}$	20,040 Hz	20,040 Hz
Current loop proportional gain $k_\mathrm{p,i}$	-	3.83 Ω
Current loop integral gain $k_\mathrm{i,i}$	-	5000 Ω/s
Voltage loop proportional gain $k_\mathrm{p,v}$	-	0.05 $\Omega^{-}1$
Voltage loop integral gain $k_\mathrm{i,v}$	75.4 Hz	3.42 $(\Omega \cdot s)^{-}1$

The block diagrams for the double-loop control strategy are presented in Figure 16. Figure 16a presents the current loop block diagram. As observed, the moving average filter is not considered in the current loop. This fact is justified because this control loop must be quite faster than the voltage control loop. To deal with the high frequency ripple, the sampling can be synchronized with the PWM carrier. Under such conditions, the current is sampled in the average value, as described in [25]. Then, the open-loop transfer function for current control is given by:

$$G_\mathrm{I}(s) = D_\mathrm{I}(s) G_\mathrm{d}(s) G_\mathrm{id}(s), \tag{23}$$

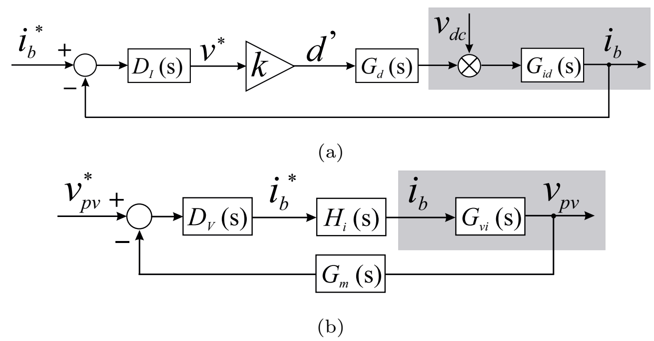

Figure 16: Block diagrams of the double-loop control scheme: (a) Current control loop; (b) Voltage control loop. In this subsection, $v_{\mathrm{dc}} = v_{\mathrm{dc}}^*$ is assumed, i.e. $kv_{\mathrm{dc}} = 1$

where $D_{\mathrm{I}}(s)$ is the current compensator. A proportional-integral controller is employed. Accordingly:

$$D_{\mathrm{I}}(s) = k_{\mathrm{p,i}} + \frac{k_{\mathrm{i,i}}}{s}, \tag{24}$$

where $k_{\mathrm{p,i}}$ is the proportional gain and $k_{\mathrm{i,i}}$ is the integral gain.

Finally, the complete block diagram for the voltage control loop is presented in Figure 16b. The open-loop transfer function is given by:

$$G_{\mathrm{V}}(s) = D_{\mathrm{V}}(s)H_{\mathrm{i}}(s)G_{\mathrm{vi}}(s)G_{\mathrm{m}}(s), \tag{25}$$

where $H_{\mathrm{i}}(s)$ is the closed loop response of the current loop, given by:

$$H_{\mathrm{i}}(s) = \frac{G_{\mathrm{I}}(s)}{1 + G_{\mathrm{I}}(s)}. \tag{26}$$

Figure 17a presents the Bode diagrams for the current loop. Uncompensated and compensated open-loop transfer function are compared. In the current control design, a high bandwidth is required. This bandwidth is limited by the switching frequency and the delay of digital implementation. Usually, values around $f_{\mathrm{sw}}/20$ are employed [26]. It is important to remark that the higher the bandwidth, the lower the phase margin. Therefore, a bandwidth around 800 Hz was adopted in this work, which leads to a phase margin around 60.8 degrees. The compensator parameters are presented in Table 4.

Figure 17b presents the Bode diagrams for the voltage loop. Because of the moving average filter, the bandwidth of the compensated system is assumed to be approximately 12 Hz (one decade below the moving average filter frequency). The obtained phase margin is around 69 degrees. The compensator parameters are presented in Table 4.

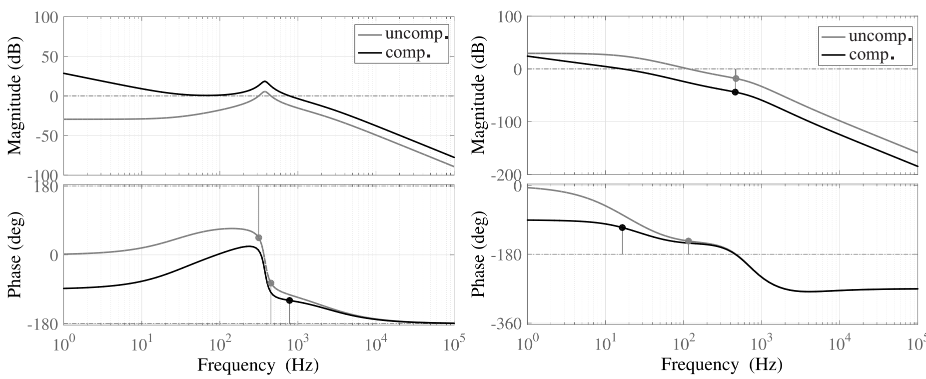

(a) (b)

Figure 17: Bode diagram of the open-loop transfer function for both uncompensated and compensated system: (a) Current control loop; (b) Voltage control loop.

The performance of the different MPPT architectures are compared through simulations of the complete model. The MPPT algorithm employed is the traditional P&O algorithm [21] The adopted parameters are $f_{\text{mpp}} = 10$ Hz and $\Delta_{\text{v}} = 3$ V. All the controllers are discretized by the Tustin (trapezoidal) method. The delay of the digital implementation is included in the model.

The results were obtained for $G = 400$ W/m^2 and $T = 32.5$ °C. This temperature was computed based on equation (7). The results for the open-loop and the single-loop schemes are presented in Figure 18a. The results for the open-loop and the double-loop schemes are presented in Figure 18b. The voltage presents steps in steady state each 0.1 seconds because of the MPPT algorithm, which oscillates around the maximum power point voltage (240.8 V for the considered operation conditions). In addition, a high frequency ripple (due to the converter switching) is observed in the waveforms.

As observed in Figure 18a and 18b, the closed-loop control improves the transient performance of the PV panel, providing a damping in the oscillations observed in the open-loop strategy. For the adopted design parameters, a slight overshoot is observed in the double-loop control scheme. This overshoot is related with the iterations between the outer and inner loop which cannot be fully eliminated, even considering quite different bandwidths.

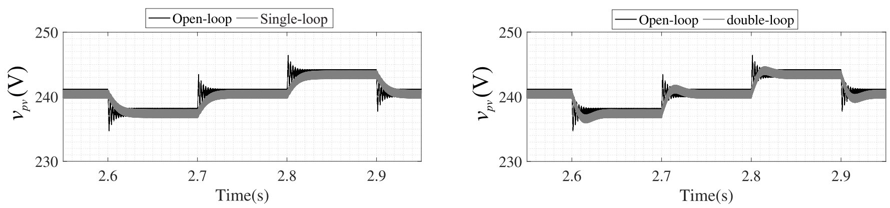

(a) (b)

Figure 18: PV array voltage response for different MPPT architectures: (a) Open-loop versus single-loop control; (b) Open-loop versus double-loop control. Operating conditions: $G = 400$ W/m^2 and $T = 32.5$ °C. MPPT algorithm parameters: $f_{\mathrm{mpp}} = 10$ Hz and $\Delta_{\mathrm{v}} = 3$ V.

5.3. Effect of the dc-ac stage operation

In section 5.2, $v_{\mathrm{dc}} = v_{\mathrm{dc}}^{*}$ was assumed. However, the dc-link voltage usually presents a low-frequency ripple, which can directly affect the MPPT performance. The low-frequency ripple is generated by the following phenomena:

- Single-phase power injection;
- Unbalanced conditions in three-phase inverters;
- Ancillary services such as harmonic compensation. This phenomenon was recently discussed in [7].

In single-stage PV inverters, the voltage ripple appears in the PV array voltage. On the other hand, when the control schemes of Fig. 11 are employed, this effect is also observed in two-stage inverters. The low-frequency voltage ripple leads to a power ripple. Thus, the performance of the maximum power point tracker is degraded, as illustrated in Fig. 19.

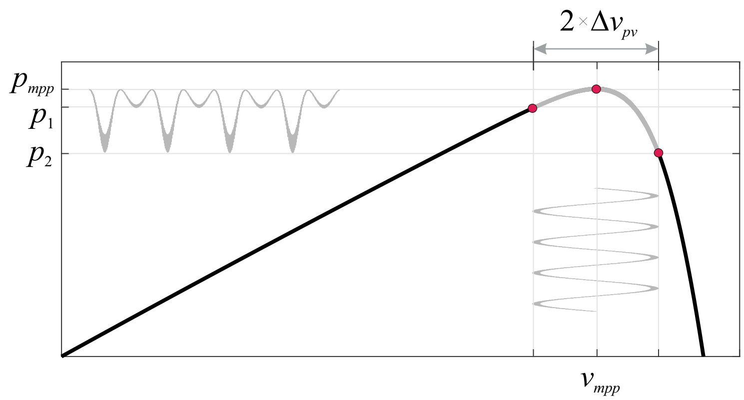

Figure 19: Effect of the solar array voltage ripple in the MPPT performance.

Initially, this section intends to discuss mathematically this problem. Then, active solutions for low-frequency ripple mitigation for two-stage PV inverters are presented. For simplicity, a single-phase PV inverter is selected as an example. In the following analyzes, the switching harmonics are neglected. The grid voltage and dc/ac stage output current are assumed to be given by:

$$v_{\mathrm{g}} = \widehat{V}_{\mathrm{g}} \cos\left(\omega_{\mathrm{n}} t\right), \tag{27}$$

$$i_{\mathrm{g}} = \widehat{I}_{\mathrm{g}} \cos\left(\omega_{\mathrm{n}} t - \varphi\right), \tag{28}$$

where ω_{n} is the grid angular frequency and φ is the displacement angle between voltage and current. The instantaneous power delivered to the grid is given by:

$$p_{\mathrm{g}} = \bar{p}_{\mathrm{g}} + \tilde{p}_{\mathrm{g}} = v_{\mathrm{g}} i_{\mathrm{g}} = \frac{\widehat{V}_{\mathrm{g}} \widehat{I}_{\mathrm{g}}}{2} + \frac{\widehat{V}_{\mathrm{g}} \widehat{I}_{\mathrm{g}}}{2} \cos\left(2\omega_{\mathrm{n}} t - \varphi\right). \tag{29}$$

Neglecting the power losses and assuming that the dc-link capacitor absorbs all the second-harmonic power oscillation yields:

$$v_{\mathrm{dc}} C_{\mathrm{dc}} \frac{d v_{\mathrm{dc}}}{dt} = \tilde{p}_{\mathrm{g}}. \tag{30}$$

An approximate solution of (30) can be found if the capacitor ripple is assumed to be small. Under such conditions:

$$v_{\mathrm{dc}} C_{\mathrm{dc}} \frac{dv_{\mathrm{dc}}}{dt} \approx v_{\mathrm{dc}}^{*} C_{\mathrm{dc}} \frac{dv_{\mathrm{dc}}}{dt} = \tilde{p}_{\mathrm{g}}. \tag{31}$$

where v_{dc}^{*} is the dc-link voltage reference. Solving (31) to v_{dc} leads to:

$$v_{\mathrm{dc}} = v_{\mathrm{dc}}^{*} + \underbrace{\frac{\widehat{V}_{\mathrm{g}} \widehat{I}_{\mathrm{g}}}{4\omega_{\mathrm{n}} C_{\mathrm{dc}} v_{\mathrm{dc}}^{*}}}_{\Delta V_{\mathrm{dc}}} \sin\left(2\omega_{\mathrm{n}} t - \varphi\right). \tag{32}$$

As observed, a second-harmonic voltage ripple is expected in single-phase inverters. Assuming that the boost converter elements are designed to attenuate only high frequency components and neglecting the power losses in the dc/dc converter, the instantaneous relation between the solar array voltage v_{pv} and dc-link voltage v_{dc} can be approximated by:

$$v_{\mathrm{pv}} \approx D^{'} v_{\mathrm{dc}}, \tag{33}$$

where $D^{'} = \frac{v_{\mathrm{pv}}^{*}}{v_{\mathrm{dc}}^{*}}$. v_{pv}^{*} is the maximum power point voltage. Under such conditions, the solar array voltage can be approximated by:

$$v_{\mathrm{pv}} = v_{\mathrm{pv}}^{*} + \underbrace{\frac{d^{'} \widehat{V}_{\mathrm{g}} \widehat{I}_{\mathrm{g}}}{4\omega_{\mathrm{n}} C_{\mathrm{dc}} v_{\mathrm{dc}}^{*}}}_{\Delta v_{\mathrm{pv}}} \sin\left(2\omega_{\mathrm{n}} t - \varphi\right). \tag{34}$$

At this point, the following conclusions can be stated:

- The dc-link voltage ripple increases when the output current (processed power) increases;
- The dc-link voltage ripple can be reduced by increasing the capacitance C_{dc}. However, the higher the capacitance, the higher the volume and the higher the cost;
- The PV array voltage ripple is proportional to $D^{'}$, i.e., the lower the v_{pv}^{*}, the higher the ripple;
- The perceptual value of PV array voltage ripple is equal to the perceptual dc-link voltage ripple.

As previously mentioned, $v_{\mathrm{dc}} = v^*_{\mathrm{dc}}$ is assumed in section 5.2. Therefore, the low-frequency ripple is neglected. One way to solve this problem is to replace the gain $k = 1/v^*_{\mathrm{dc}}$ by a real-time normalization by the v_{dc} measurement, as shown in Figure 20a. This scheme can be understood as a linearization of the boost converter control plant. In theory, this technique leads to a ripple-free waveform in v_{pv}. However, this is not observed in practice because of the delay caused by the PWM modulator and digital implementation. Indeed, this ripple mitigation strategy operates essentially in open loop.

An alternative to the plant linearization scheme is the closed-loop control presented in Figure 20b. In this approach, a harmonic controller (HC) is included in the control algorithm. The principle is to remove the low-order harmonics from v_{pv}. The compensator HC is usually a repetitive of a multi-resonant controller. In the case discussed in this section, a second-harmonic ripple is observed in the capacitor voltage. Therefore, a single resonant controller tuned in the second harmonic is employed. Accordingly:

$$HC(s) = \frac{k_{\mathrm{r}}}{s^2 + 4\omega_{\mathrm{n}}^2}. \tag{35}$$

where k_{r} is the resonance controller. It is important to remark that the control schemes Figure 20a and 20a can be combined.

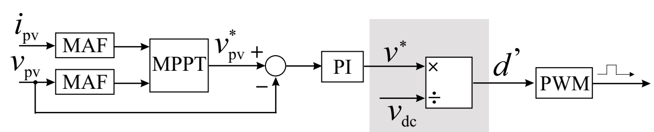

(a)

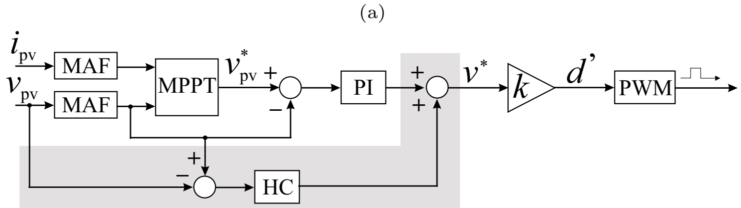

(b)

Figure 20: Ripple mitigation strategies for single-loop control schemes: (a) Scheme based on plant linearization; (b) Scheme based on harmonic controller.

The performance of ripple mitigation strategies is presented in Figure 21 considering the parameters of Table 3. The resonant controller is discretized by the Tustin with pre-warping method, as described in [27]. The results were obtained for $G = 1000$ W/m^2 and $T = 51.25$ °C. This temperature was computed based on equation (7). The plant linearization and plant linearization + harmonic controller schemes are compared. A dc-link voltage with 10 % second-harmonic ripple is simulated, as shown in Figure 21a. At t = 3 seconds, the plant linearization scheme is activated. At t = 3.5 seconds, the plant linearization and the harmonic controller are activated.

As observed in Figure 21b, when the traditional control scheme is employed, the solar array voltage v_{pv} presents a significant second-order harmonic ripple. In addition, the dc/dc converter duty-cycle is approximately constant, as shown in Figure 21c. The voltage ripple in Δv_{pv} is approximately 10 %, as predicted by equation (34).

When the plant linearization scheme is activated, the voltage ripple is strongly reduced, as shown in Figure 21b. As expected, the converter duty-cycle presents a pulsation attenuating the ripple in v_{pv}, as presented in Figure 21c. Nevertheless, the plant linearization scheme cannot cancel the second-harmonic ripple in the solar array voltage. At $t = 3.5$ seconds the harmonic controller is activated. As observed, the combination of the plant linearization and the harmonic controller can remove the second-harmonic ripple in v_{pv} without affecting the voltage control dynamic performance.

Figure 21d presents the solar array power. The different peaks observed in the solar array power are related to the different derivatives of the P - V before and after the maximum power point voltage, as shown in Figure 19. The voltage oscillation leads to power oscillations and degrades the MPPT performance. When the ripple mitigation strategies are used, the power oscillations are practically canceled.

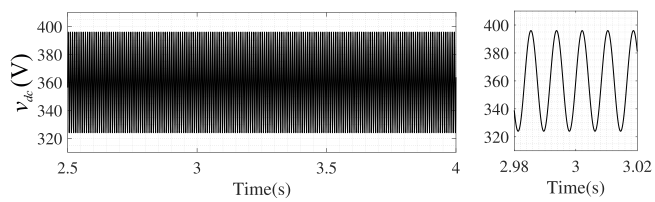

(a)

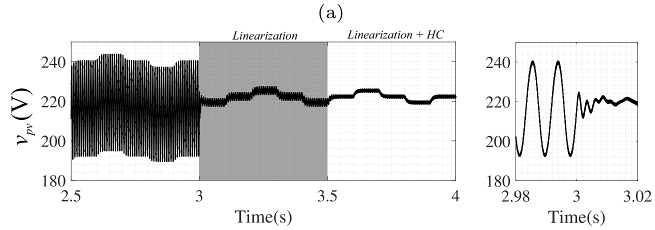

(b)

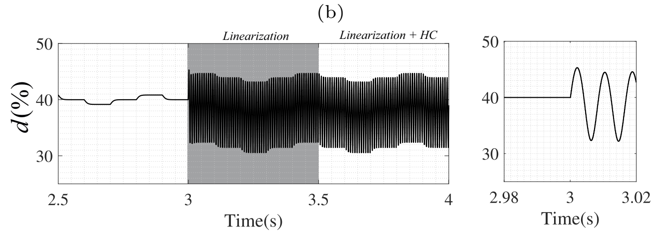

(c)

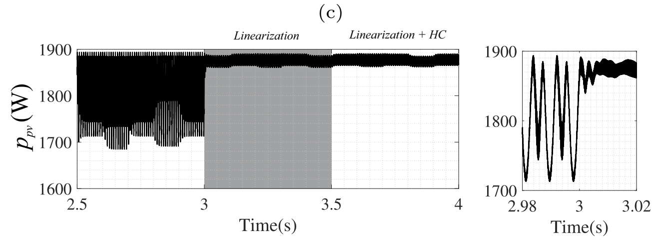

(d)

Figure 21: Performance of the ripple mitigation strategies in a two-stage single-phase PV inverter: (a) Dc-link voltage; (b) PV array voltage; (c) Dc/dc converter duty-cycle; (d) PV array power.

6. Dc/ac stage modelling and control in single-phase systems

6.1. Architectures

The dc/ac stage dynamic behavior depends on the output filter architecture of the inverter. This filter attenuates the harmonics generated by the inverter switching according to the standards. Initially, pure inductive filters (L) were employed due to its simplicity, as presented in Figure 22a. However, the first-order characteristic leads to high value of inductance, which generates a high voltage drop and increases the inverter volume and weight.

LC filter was proposed as an alternative to single L filter, as shown in Figure 22b. The second-order filtering characteristic increases the attenuation for high frequencies and reduces filter volume. A drawback of this topology is the dependence of resonance frequency with the grid impedance, which affects the stability of the current control [26]. Other issue is the capacitor inrush current when the inverter is connected to the grid.

LCL topology is a third-order filter, which gained attention is last 10 years as an alternative to LC filters. This topology is shown in Figures 22c and 22d. This approach reduces both volume and voltage drop through the inductors, if compared to the L and LC topologies. Furthermore, the second inductance limits the capacitor inrush current and increases the robustness against grid inductance variation. However, the inherent resonance frequency of the LCL filter also hinders current control tuning.

Different measurement schemes can be adopted in single-phase PV inverters, as shown in Figure 22. The following points must be remarked:

- The dc-link voltage measurement is included in all commercial systems based on voltage-source converters, because the dc-link voltage control is required to the correct operation of the PV inverter;
- The grid voltage measurement is employed in practically all commercial systems. Usually, it is performed after the disconnection relays, as shown

in Figure 22 [7]. Therefore, the grid voltage can be monitored, and the synchronization is reached before connecting the inverter to the grid;

- When L filters are employed, only the output current and output voltage are measured, as shown in Figure 22a;
- When LC filters are employed, the scheme presented in Figure 22b is employed;
- When LCL filters are employed, different measurement schemes are possible. Figure 22c shows a strategy where the inverter current is controlled. On the other hand, Figure 22d shows a strategy where the output current is controlled.

The architectures presented in Figure 22b - 22d assume that the grid impedance does not affect the stability of LC and LCL filters current control. However, commercial inverters can be connected in different places and stability issues arise, mainly when weak grid conditions are considered. The stability of LCL filter-based systems is also affected by the controlled current (inverter or grid current). This problem is reported in many works in literature and several damping methods are proposed to solve this problem.

Indeed, the delay caused by the digital implementation of current control can generate an inherent damping in the current control of PV inverters with LCL filter. Assuming equal switching and sampling frequencies, the stability is directly affected by following ratio:

$$r_{\mathrm{f}} = \frac{f_{\mathrm{sw}}}{f_{\mathrm{res}}}, \tag{36}$$

[7] The commercial PV inverters must have a disconnection structure to perform the anti-islanding protection. Usually, two redundant relays commanded by independent controllers are employed.

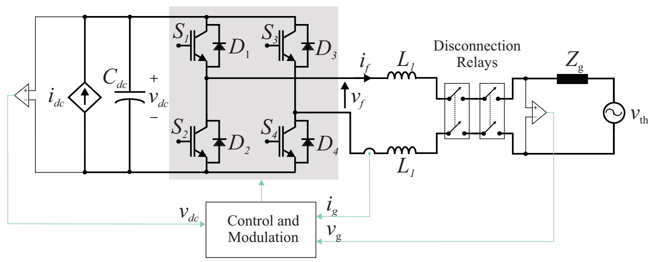

(a)

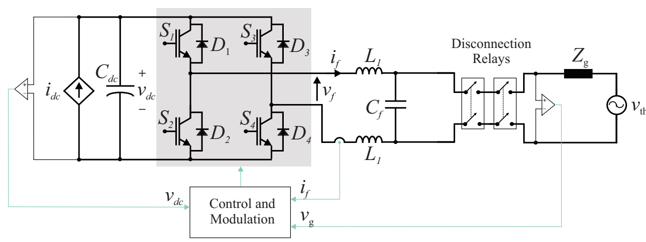

(b)

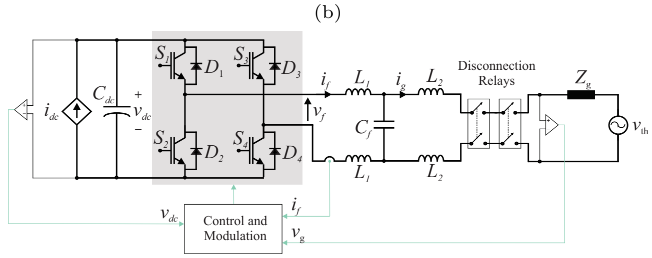

(c)

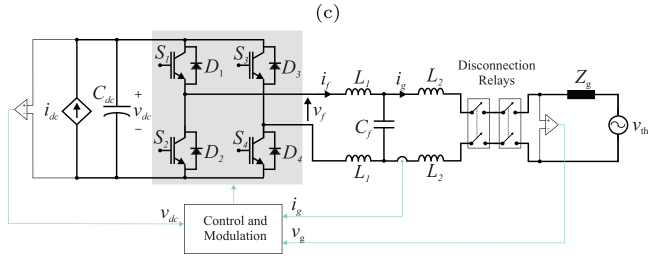

(d)

Figure 22: Different measurement schemes for single-phase PV inverters: (a) PV inverter with L filter; (b) PV inverter with LC filter; (c) PV inverter with LCL filter and inverter current control; (d) PV inverter with LCL filter and grid current control. Z_g represents the equivalent grid impedance. It is important to remark that other measurements can be included to increase the robustness against weak grid conditions.

where f_{sw} is the switching frequency and f_{res} is the LCL filter resonance frequency, given by:

$$f_{\mathrm{res}} = \frac{1}{2\pi}\sqrt{\frac{1}{C_{\mathrm{f}}}\left(\frac{1}{L_{\mathrm{f}}} + \frac{1}{L_{\mathrm{g}}}\right)}, \tag{37}$$

where $L_{\mathrm{f}} = 2L_1$, $L_{\mathrm{g}} = 2L_2$. The inherent damping characteristics of LCL filters were investigated by [28]. According to this reference, the converter and grid current control present complementary behaviors in terms of stability. Moreover, there is always one current control that is inherently stable without damping. If the value of r_{f} is in the the range $2 < r_{\mathrm{f}} < 6$, the grid current control is inherently stable, while for inverter current control the damping is essential to reach stability. On the other hand, if $r_{\mathrm{f}} > 6$ or $r_{\mathrm{f}} < 2$, the inverter current feedback is stable, while for the grid current feedback, a damping strategy is necessary to reach stability. It is important to highlight that the region $r_{\mathrm{f}} < 2$ is not recommended in practical designs, since it reduces filter attenuation at the switching frequency. Additionally, the variations in the filter parameters and weak grid conditions justify the use of damping strategies in both grid and converter current feedback [26].

Indeed, the damping strategies for LC and LCL filters are quite similar. In [26], the authors presented a comprehensive review of different damping strategies for grid-connected inverters with LCL filter. This reference classifies the strategies as passive and active damping. The passive damping inserts passive elements in the filter structure. The most adopted approach is to insert a resistor in series with the filter capacitor. As drawbacks, the resistor increases the energy losses and reduces the filter attenuation.

For this reason, active damping strategies have been developed. As advantages, the filter attenuation and power losses are not affected. The damping is performed through the digital control algorithm. Among the active damping strategies, notch filter-based active damping (NF) is proposed [26]. As advantages, no additional measurements are required. However, the robustness against variations in the filter parameters and weak grid conditions is a challenge.

The capacitor current feedback (CCF) and capacitor voltage feedback (CVF) strategies are other active damping strategies. However, additional measurements are required. CCF leads to higher costs than CVF since current measurement is more expensive than voltage measurement. On the other hand, capacitor voltage feedback requires the digital implementation of a derivative, which is another challenge investigated in literature [26].

6.2. Control Schemes

Regarding the control schemes, reference [5] presents a comprehensive review of different control schemes for PV inverters. Figure 23 summarizes the most common control algorithms implemented in commercial single-phase PV inverters [8]. As observed, a cascade control structure is employed. The outer loops control the dc-link voltage and reactive power while the inner loops control the current injected into the grid.

Figure 23a and 23b presents the control strategy based on the natural reference frame. In these strategies, the current reference is sinusoidal and traditional proportional integral (PI) controllers cannot guarantee zero steady-state error. Therefore, proportional resonant (PR) controllers are used in the current control loop. In the dc-link voltage control, proportional integral controllers are used. Moving average filters are employed to remove the low-frequency ripple in the dc-link, as discussed in Section 5.3. Finally, a feedforward of the PV array power p_{pv} is employed to improve dynamic performance.

Two approaches can be adopted for dc-link voltage control: control the dc-link voltage, as shown in Figure 23a or control the square of the dc-link voltage, as shown in Figure 23b. In the case of the Figure 23a, the outer loops compute the current in the synchronous reference frame $i_{\mathrm{g,d}}$ and $i_{\mathrm{g,q}}$. Then, the reference current is obtained as:

[8] Although the grid current control is represented, similar structures can be used for the inverter current control. In addition, active damping schemes are not showed in this basic control diagram. For my details on this topic, see [26].

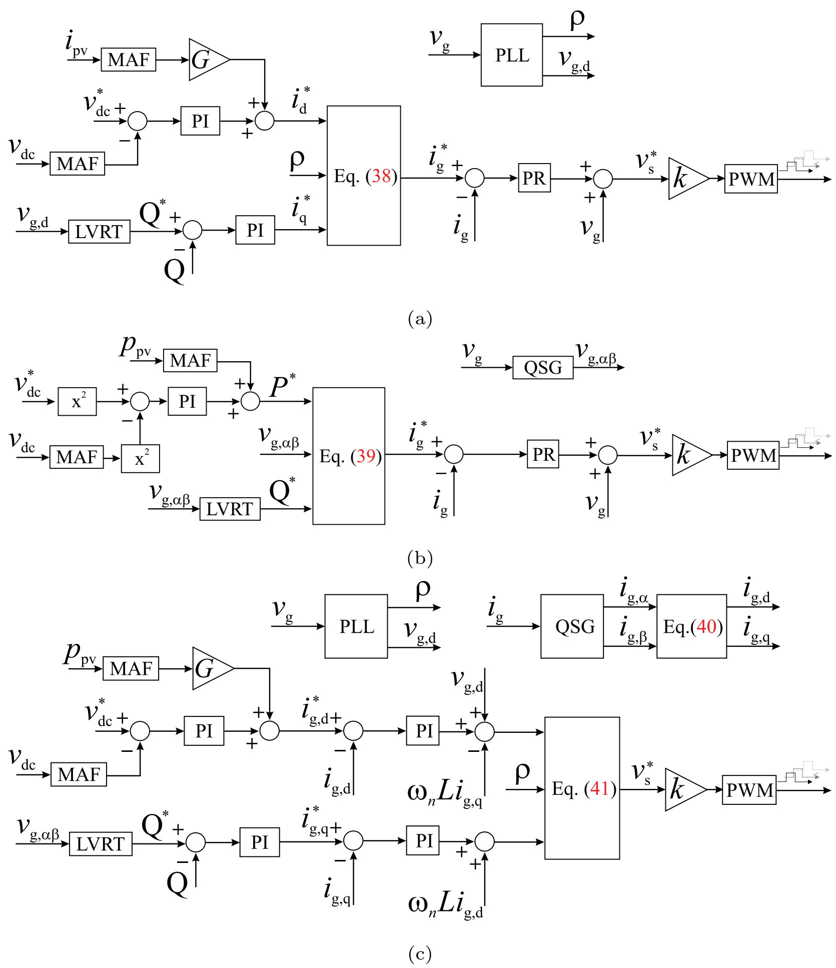

Figure 23: Control architectures for single-phase PV inverters: (a) Control in natural reference frame with v_{dc} control; (b) Control in natural reference frame with v_{dc}^2 control; (c) Control in synchronous reference frame with v_{dc} control. $L = L_{\mathrm{f}} + L_{\mathrm{g}}$ and $k = \frac{1}{v_{\mathrm{dc}}^*}$. QSG means quadrature signal generator, PLL means phase-locked loop and LVRT means low-voltage ride through.

$$i_{\mathrm{g}}^* = i_{\mathrm{g,d}} \cos \rho - i_{\mathrm{g,q}} \sin \rho, \tag{38}$$

where $\rho = \omega_{\mathrm{n}} t$ is the grid voltage angle. This variable is usually estimated by a phase-locked loop (PLL) algorithm.

On the other hand, the control of the square dc-link voltage computes the active power reference P^*. In this case, the current reference is computed as follows:

$$i_{\mathrm{g}}^* = \frac{2v_{\mathrm{g},\alpha}}{v_{\mathrm{g},\alpha}^2 + v_{\mathrm{g},\beta}^2}P^* + \frac{2v_{\mathrm{g},\beta}}{v_{\mathrm{g},\alpha}^2 + v_{\mathrm{g},\beta}^2}Q^*, \tag{39}$$

Q^* is the reactive power reference and $v_{\mathrm{g},\alpha}$ and $v_{\mathrm{g},\beta}$ are obtained from the grid voltage through a quadrature signal generator (QSG) structure.

Finally, Figure 23c presents the synchronous reference frame control. In this approach, the novelty is the Park transformation:

$$\begin{bmatrix} X_{\mathrm{d}} \\ X_{\mathrm{q}} \end{bmatrix} = \begin{bmatrix} \cos\rho & \sin\rho \\ -\sin\rho & \cos\rho \end{bmatrix} \begin{bmatrix} X_\alpha \\ X_\beta \end{bmatrix}, \tag{40}$$

where X can represent a current or voltage. The components X_α and X_β are obtained from a quadrature signal generator (QSG). A PLL is also required to estimate ρ.

Because of the Park transformation, the controlled signals are dc. Therefore, conventional proportional-integral controllers can be employed. However, additional decoupling terms are necessary to guarantee independent active and reactive power control. Finally, the reference voltage for the PWM modulator is computed based on the inverse Park transformation as follows:

$$\begin{bmatrix} X_\alpha \\ X_\beta \end{bmatrix} = \begin{bmatrix} \cos\rho & -\sin\rho \\ \sin\rho & \cos\rho \end{bmatrix} \begin{bmatrix} X_{\mathrm{d}} \\ X_{\mathrm{q}} \end{bmatrix}, \tag{41}$$

The reactive power reference is usually computed according to the low-voltage ride through (LVRT) required by the modern grid codes. Most of them require a reactive current profile given by Figure 24. This profile is based on reactive current, because the transferred reactive power is a function of the grid voltage. If $\widehat{V}_{\mathrm{g}}$ (peak of grid voltage) is higher than 1 pu (per unit), inductive reactive current is provided by the inverter until the maximum voltage limit $\widehat{V}_{\mathrm{max}}$. On the other hand, if the voltage is lower than $\widehat{V}_{\mathrm{lim}}$, capacitive reactive current is provided by the inverter. The droop lines present a slope $H = \tan\theta_1 = \tan\theta_2$. When the voltage is lower than $\widehat{V}_{\mathrm{lim}}$, all the capacity of the converter must be used for reactive power injection. Finally, if the voltage is higher than $\widehat{V}_{\max}$ or lower than $\widehat{V}_{\text{lim}}$ for a certain period of time, the inverter can be disconnected from the grid. Regarding typical values, $\widehat{V}_{\max} = 1.2$ pu, $0.8 \leq \widehat{V}_{\text{lim}} \leq 0.9$ pu, $2 \leq H \leq 10$ and $\widehat{V}_{\min} = 0.5$ pu are adopted [29].

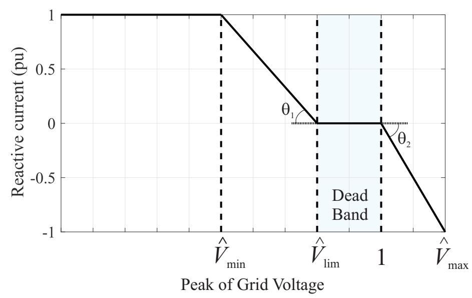

Figure 24: General reactive current injection profile for modern grid codes.

The control scheme presented in Figure 23b is discussed in this Chapter. The strategy presents the following advantages:

- The control of the square of dc-link voltage includes a normalization by the grid voltage amplitude, as shown in equation (39). Therefore, the dynamics of the dc-link voltage is improved during voltage sags in comparison with the schemes of Figures 23a and 23c;

- This strategy does not require the park transformations and decoupling terms required in Figure 23c;

- The control of the square of dc-link voltage presents explicitly the active power reference, which is useful for current dynamic saturation purposes (discussed in the next sections).

On the other hand, two drawbacks can be identified in the control algorithm of Figure 23b:

- The reactive power is in open-loop. Under such conditions, small phase errors in current control can lead to steady-state errors in the reactive power;

- When the modulation signal is normalized by v_{dc}^{*}, the interaction between the second-order dc-link voltage ripple and the fundamental frequency modulation signals leads to a third-harmonic current in the grid current, as investigated by reference [30].

Therefore, this chapter proposes improvements in the original control strategy shown in Figure 23b. The improved control scheme is presented in Figure 25. As observed, a scheme like that shown in section 5.3 is employed to suppress the third-harmonic current. In addition, a reactive power control loop is added to eliminate the steady-state error. The next sections present the dynamic modelling and the control tuning of the proposed strategy.

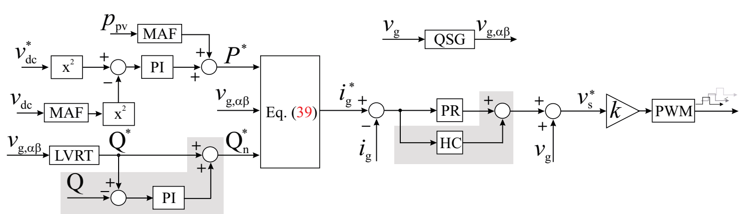

Figure 25: Proposed control for single-phase PV inverters based on v_{dc}^{2} control and natural reference frame current control.

6.3. Dynamic modelling and control tuning

The dynamic modelling of the dc/ac stage is divided into current and dc-link voltage dynamics. In the current dynamic modelling, the dc-link is assumed to be constant. Therefore, the average model presented in Figure 26a is obtained. Under such conditions, the following dynamic equations can be obtained:

$$\begin{cases} v_{\mathrm{s}} - L_{\mathrm{f}}\frac{di_{\mathrm{f}}}{dt} - R_{\mathrm{f}}i_{\mathrm{f}} = v_{\mathrm{C_f}}, \\ v_{\mathrm{C_f}} - L_{\mathrm{g}}\frac{di_{\mathrm{g}}}{dt} - R_{\mathrm{f}}i_{\mathrm{g}} = v_{\mathrm{g}}, \\ i_{\mathrm{f}} - i_{\mathrm{g}} = C\frac{dv_{\mathrm{C_f}}}{dt} \end{cases} \tag{42}$$

where v_{s} is the fundamental voltage synthesized at the converter output.

Using these dynamic equations and applying the Laplace transform, the following transfer functions can be obtained:

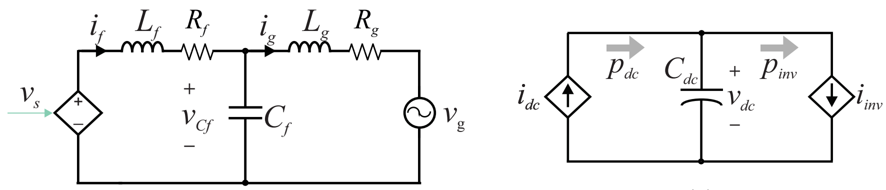

(a) (b)

Figure 26: Average model of the dc/ac converter: (a) Average model of output current dynamics; (b) Average model of the dc-link dynamics.

$$\frac{I_{\mathrm{f}}(s)}{V_{\mathrm{s}}(s)} = \frac{s^2 C_{\mathrm{f}} L_{\mathrm{g}} + s C_{\mathrm{f}} R_{\mathrm{g}} + 1}{s^3 C_{\mathrm{f}} L_{\mathrm{g}} L_{\mathrm{f}} + s^2 C_{\mathrm{f}} (L_{\mathrm{f}} R_{\mathrm{g}} + L_{\mathrm{g}} R_{\mathrm{f}}) + s(C_{\mathrm{f}} R_{\mathrm{g}} R_{\mathrm{f}} + L_{\mathrm{f}} + L_{\mathrm{g}}) + R_{\mathrm{f}} + R_{\mathrm{g}}} \tag{43}$$

$$\frac{I_{\mathrm{g}}(s)}{V_{\mathrm{s}}(s)} = \frac{1}{s^3 C_{\mathrm{f}} L_{\mathrm{g}} L_{\mathrm{f}} + s^2 C_{\mathrm{f}} (L_{\mathrm{f}} R_{\mathrm{g}} + L_{\mathrm{g}} R_{\mathrm{f}}) + s(C_{\mathrm{f}} R_{\mathrm{g}} R_{\mathrm{f}} + L_{\mathrm{f}} + L_{\mathrm{g}}) + R_{\mathrm{f}} + R_{\mathrm{g}}} \tag{44}$$

Since the current control plant is a third-order system, the control tuning is not straightforward. A common approximation for controller tuning in LC and LCL filters is assume that the effect of the capacitor is negligible around the fundamental frequency. Therefore, LC and LCL filters are reduced to L filters and simple tuning formulas can be obtained. A mathematical proof of this concept can be obtained based on the Padé approximant. The Padé approximant of a function $f(x)$, denoted by $p_{\mathrm{M,N}}(x)$ consists of a quotient of two polynomials with numerator degree N and denominator M, where $N > M$. Since $N > M$, the Padé approximant must be computed based on the inverse of the transfer functions (43) and (44). Therefore, the Padé approximant in low-frequency region ($\omega \to 0$) is given by:

$$p_{\mathrm{f}_{\mathrm{M,N}}} = s(L_{\mathrm{f}} + L_{\mathrm{g}} - C_{\mathrm{f}} R_{\mathrm{g}}^2) + R_{\mathrm{f}} + R_{\mathrm{g}}, \tag{45}$$

$$p_{\mathrm{g}_{\mathrm{M,N}}} = s(L_{\mathrm{f}} + L_{\mathrm{g}} + C_{\mathrm{f}} R_{\mathrm{f}} R_{\mathrm{g}}) + R_{\mathrm{f}} + R_{\mathrm{g}}. \tag{46}$$

If the high-order terms $C_\mathrm{f} R_\mathrm{g}^2$ and $C_\mathrm{f} R_\mathrm{f} R_\mathrm{g}$ are neglected, the transfer functions (43) and (44) can be simplified as follows:

$$\frac{I_\mathrm{f}(s)}{V_\mathrm{s}(s)} \approx \frac{1}{sL_\mathrm{eq} + R_\mathrm{eq}}, \tag{47}$$

$$\frac{I_\mathrm{g}(s)}{V_\mathrm{s}(s)} \approx \frac{1}{sL_\mathrm{eq} + R_\mathrm{eq}}. \tag{48}$$

where $L_\mathrm{eq} = L_\mathrm{f} + L_\mathrm{g}$ and $R_\mathrm{eq} = R_f + R_\mathrm{g}$. Therefore, the current control can be represented by the block diagram of Figure 27. The current compensator is a proportional resonant controller given by:

$$D_\mathrm{cc}(s) = k_\mathrm{p,cc} + \frac{k_\mathrm{r,cc} s}{s^2 + \omega_\mathrm{n}^2} + \frac{k_\mathrm{r,cc} s}{s^2 + 9\omega_\mathrm{n}^2}, \tag{49}$$

where the last resonant term is included to suppress the third-harmonic current in the inverter output. Therefore, the following open-loop transfer function is obtained:

$$G_\mathrm{i}(s) = \left(k_\mathrm{p,cc} + \frac{k_\mathrm{r,cc} s}{s^2 + \omega_\mathrm{n}^2} + \frac{k_\mathrm{r,cc} s}{s^2 + 9\omega_\mathrm{n}^2}\right) \frac{1}{1.5T_\mathrm{sw} s + 1} \frac{1}{L_\mathrm{eq} s + R_\mathrm{eq}}. \tag{50}$$

As observed, the implementation delay is approximated by equation (18). Reference [31] discusses the optimum design of the PR controllers for grid current control. The methodology proposes to maximize the control bandwidth for a given desired phase margin ϕ_m (e.g. 85 degrees). This approach leads to the following tuning formulas:

$$k_\mathrm{p,cc} = \frac{\pi/2 - \phi_\mathrm{m}}{1.5T_\mathrm{sw}} L_\mathrm{eq}, \tag{51}$$

$$k_\mathrm{r,cc} = \frac{(\pi/2 - \phi_\mathrm{m})}{15T_\mathrm{sw}} k_\mathrm{p,cc}. \tag{52}$$

On the other hand, the dynamics of the dc-link voltage can be obtained based on the energy stored (W) given by:

$$W = \frac{1}{2} C_\mathrm{dc} v_\mathrm{dc}^2. \tag{53}$$

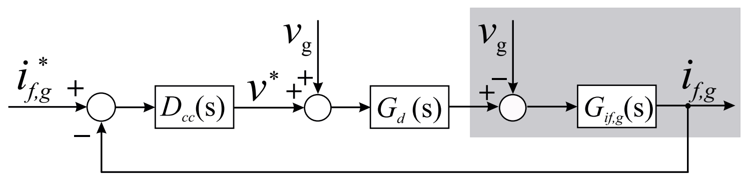

Figure 27: Block diagram of the current control.

The time derivative of the W represents the instantaneous power developed in the capacitor terminals. According to the Figure 26b, the following equation can be obtained [32]:

$$\frac{dW}{dt} = p_{\mathrm{dc}} - p_{\mathrm{inv}}. \tag{54}$$

Replacing (53) in (54) yields:

$$\frac{dv_{\mathrm{dc}}^2}{dt} = \frac{2}{C_{\mathrm{dc}}}\left(p_{\mathrm{dc}} - p_{\mathrm{inv}}\right). \tag{55}$$

Therefore, considering $y = v_{\mathrm{dc}}^2$ and applying the Laplace transform, the following transfer function can be obtained:

$$Y(s) = \frac{2}{sC_{\mathrm{dc}}}\left(P_{\mathrm{dc}}(s) - P_{\mathrm{inv}}(s)\right). \tag{56}$$

Therefore, the block diagram illustrated in Figure 28 is obtained. Assuming that the power feedforward cancels the term p_{dc} and $G_{\mathrm{cc}} \approx 1$ (i.e., a quite fast current control loop), the following open-loop transfer function is obtained:

$$OL_{\mathrm{v}}(s) = k_{\mathrm{p,dc}} \frac{1 + \tau_{\mathrm{dc}} s}{\tau_{\mathrm{dc}} s} \frac{1}{0.25 T_{\mathrm{m}} s + 1} \frac{2}{C_{\mathrm{dc}} s}, \tag{57}$$

where the moving-average filter is approximated by relation (20). As observed, a proportional integral compensator is employed. The dc-link control tuning is investigated in [33]. Using the symmetrical optimum method, the following tuning formulas can be obtained [33]:

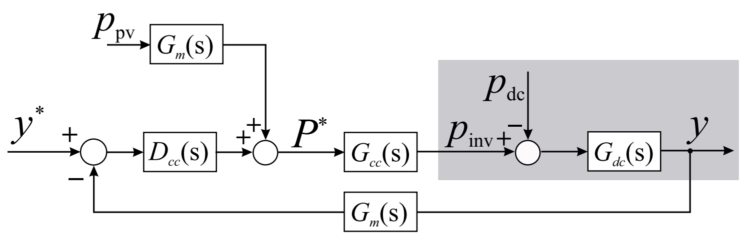

Figure 28: Block diagram of the dc-link voltage control.

$$k_{\mathrm{p,dc}} \approx 1.44 \frac{C_{\mathrm{dc}}}{T_{\mathrm{m}}}, \tag{58}$$

$$\tau_{\mathrm{dc}} \approx 1.42 T_{\mathrm{m}}, \tag{59}$$

which leads to a phase-margin of approximately 45 degrees [33].

Finally, the proposed reactive power control is analyzed. The active and reactive power in single-phase systems can be obtained by:

$$P = \frac{1}{2} \left(v_{\mathrm{g},\alpha} i_{\mathrm{g},\alpha} + v_{\mathrm{g},\beta} i_{\mathrm{g},\beta} \right), \tag{60}$$

$$Q = \frac{1}{2} \left(v_{\mathrm{g},\beta} i_{\mathrm{g},\alpha} - v_{\mathrm{g},\alpha} i_{\mathrm{g},\beta} \right). \tag{61}$$

Therefore, the power is directly affected by the injected current. When small phase errors are present in the current control, steady-state errors appear in the active and reactive power. The error of active power is eliminated by the integral action of the dc-link voltage compensator. However, this problem is observed in the reactive power when the control strategy of Figure 23c is used.

Under such conditions, this chapter proposes to remove the reactive power steady-state error based on feedback, as shown in Figure 25. The proposed scheme can be represented by the simplified block diagram of Figure 29, where $F(s)$ denotes any disturbance which causes some reactive power steady-state error. The controller is tuned considering the dynamic stiffness concept[9]. The current control loop is assumed to be fast and $G_{\mathrm{cc}} \approx 1$. If $D_{\mathrm{Q}}(s)$ is a simple integrator, the dynamic stiffness is given by:

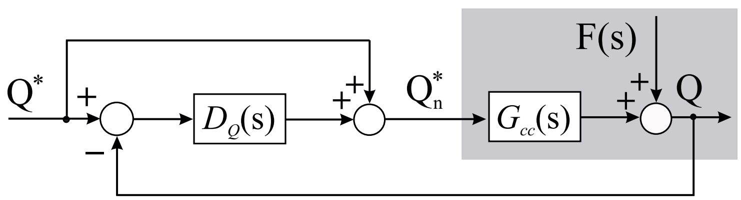

Figure 29: Block diagram of the reactive power control.

$$\frac{F(s)}{Q(s)} = 1 + \frac{k_{\mathrm{i,Q}}}{s}, \tag{62}$$

where $k_{\mathrm{i,Q}}$ is the integral gain. When $s \to 0$, the dynamic stiffness becomes high (i.e., the system becomes robust). When $s \to \infty$, the dynamic stiffness tends to one. These two asymptotes cross each other in the frequency:

$$\omega_{\mathrm{C}} = k_{\mathrm{i,Q}}. \tag{63}$$

The frequency ω_{C} must be selected to be lower than the current control loop crossover frequency. Generally the current control loop is tuned between one and two decades of the switching frequency. Therefore, a reasonable approach is to place ω_{C} three decades below the switching frequency. Therefore, the integral gain is estimated by:

[9]The dynamic stiffness is defined as the transfer function of the output considering the disturbance as input and the reference as zero. This approach is very useful to tune robust controllers.

$$k_{\mathrm{i,Q}} \approx \frac{2\pi}{1000T_{\mathrm{sw}}}. \tag{64}$$

6.4. Simulation results

The proposed control strategy is validated through simulation results. The parameters of the dc/ac stage are presented in Table 5. The boost converter parameters are the same presented in Table 3 and the single-loop strategy is employed. The tuned control gains for the dc/ac stage are shown in Table 6. The proportional integral controllers are dicretized by Tustin method, while the proportional resonant controllers are discretized by Tustin with pre-warping method.

In the presented results, the quadrature signal generator structure based on the second order generalized integrator (SOGI) is employed. More details about this QSG structure can be found in [34]. Two tests are performed. In the first test, the performance of the third-harmonic current suppression is evaluated. Then, the proposed reactive power control performance is evaluated.

Table 5: Parameters of the dc/ac stage considered in the simulations.

Parameters	Value
Dc-link capacitance C_{dc}	1200 μF
LCL filter inductance $L_{\mathrm{f}} = L_{\mathrm{g}}$	500 μH
Inductor ESR R_{L}	19 mΩ
Dc-link voltage reference v_{dc}^{*}	360 V
Switching frequency f_{sw}	20,040 Hz
Grid voltage (line-to-line RMS) V_{g}	220 V
Rated current (peak) $\widehat{I}_{\mathrm{r}}$	15 A

Table 6: Tuned compensator parameters.

Parameters	Values
Moving average filter frequency f_{m}	120 Hz
Sampling frequency $f_{\mathrm{s}} = f_{\mathrm{sw}}$	20,040 Hz
Current loop proportional gain $k_{\mathrm{p,cc}}$	1.166 Ω
Current loop resonant gain $k_{\mathrm{i,cc}}$	135.93 Ω/s
Voltage loop proportional gain $k_{\mathrm{p,dc}}$	0.2074 Ω^{-1}
Voltage loop integral gain $k_{\mathrm{i,dc}}$	17.52 $(\Omega \cdot s)^{-1}$
Reactive power loop integral gain $k_{\mathrm{i,Q}}$	125.92 Hz

Figure 30 presents the results for the third-harmonic current elimination. The results were obtained for $G = 1000$ W/m^2 and $T = 51.25$ °C. This temperature was computed based on equation (7). The third-harmonic resonant controller is activated at 3 seconds. As observed in Figure 30a, the technique is able to reduce considerably the distortion of the inverter output current. In addition, the grid current and voltage are in phase, which indicates that the inverter is injecting active power into the grid.

The dc-link voltage is presented in Figure 30b. As noted, the proposed strategy slightly reduces the dc-link voltage ripple and no significant transients are observed when the third-harmonic resonant controller is activated. Figures 30c and 30d presents the PV array voltage and power, respectively. As observed, the proposed strategy does not affect the MPPT performance. This is justified by the boost converter control proposed in section 5.3, which reduces the effect of the dc-link voltage ripple in the PV array voltage.

Figure 31 presents the results for the reactive power control. The results were obtained for $G = 1000$ W/m^2 and $T = 51.25$ °C. A ramp of reactive power (10 kvar/s) from 0 to 1500 var is applied in the reactive power reference. The results of the conventional approach (Figure 23c) and the proposed scheme (Figure 25) are compared. The third-harmonic suppression control is used in both strategies.

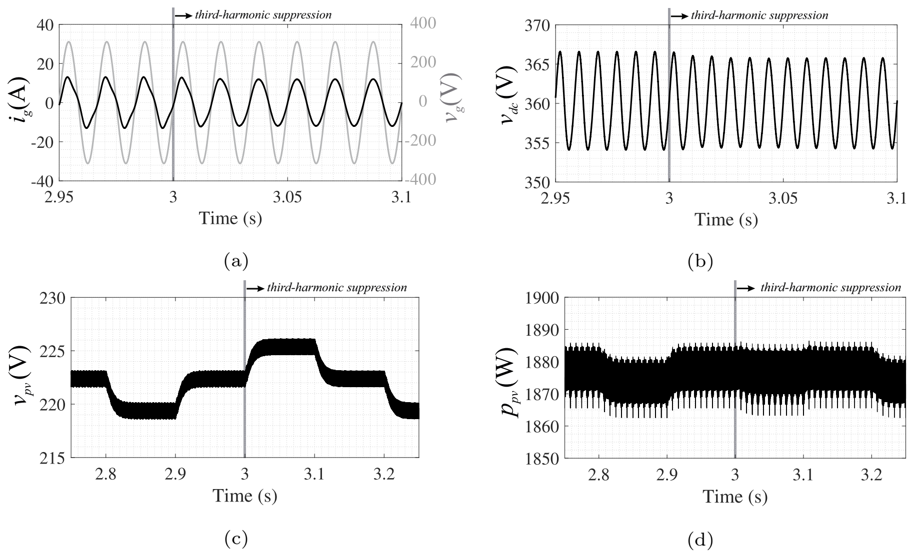

Figure 30: Simulation results of the proposed third-harmonic current suppression scheme: (a) Grid voltage and grid current; (b) Dc-link voltage; (c) PV array voltage; (d) PV array power.

Figure 31a presents the grid voltage and current. When the reactive power is injected by the inverter, the angular displacement between current and voltage changes. In addition, the current amplitude increases, because the PV inverter processes more apparent power. Figure 31b shows the reactive power injected by the inverter for the conventional and proposed control schemes. As observed, there are differences in the injected power in both transient and steady-state values. The observed differences are clarified in Figure 31c, which shows the reactive power error $\Delta Q = Q^{*} - Q$. As noticed, the conventional scheme presents non-negligible errors in transient and steady state. On the other hand, the proposed scheme guarantees a zero steady-state error in the reactive power.

6.5. Experimental results - current control

This section presents some experimental results for the grid current control. The parameters of the experimental setup are presented in Table 7. This setup presents an L filter and a dc-source is connected to the inverter dc-link. Therefore, this setup is useful to validate the current control scheme based on

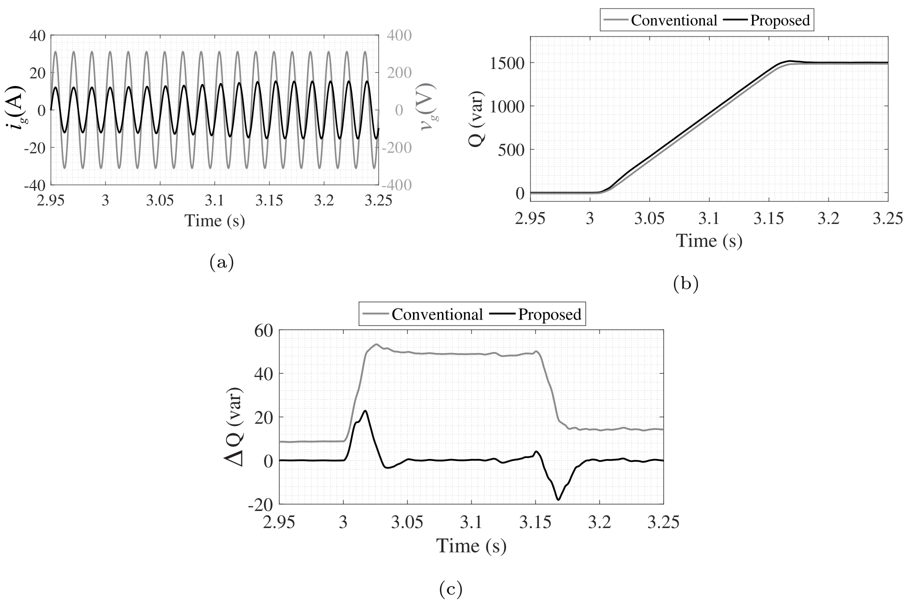

Figure 31: Simulation results of the proposed reactive power control: (a) Grid voltage and grid current; (b) Reactive power for the traditional and proposed scheme; (c) Reactive power error for the traditional and proposed scheme.

PR compensator. The PR controller was implemented in a F28335 floating-point DSP from Texas Instruments. The Tustin with pre-warping discretization method was employed.

Table 7: Parameters of experimental setup.

Parameters	Value
Grid voltage (line-to-line RMS) V_{g}	45 V
Switching frequency f_{sw}	6,000 Hz
Sampling frequency f_{s}	12,000 Hz
Dc-link voltage reference v_{dc}^{*}	60 V
L filter inductance L_{f}	8 mH
Inductor ESR R_{L}	80 mΩ

Figure 32a presents the current transient during the connection to the grid with the current reference set to zero. As observed, after two fundamental cycles the current reach steady-state. The ripple observed in the current is due to the converter switching. Figure 32b presents the grid and the inverter voltage when only active power is injected and the current reference is 2 A. As observed, the inverter voltage is a 3-level waveform, which is a characteristic of the unipolar PWM modulation employed.

Finally, Figures 32c and 32d presents the transient response during active and reactive power steps. As observed, the proportional resonant controller follows the current reference with no significant overshoot. Furthermore, the current is in phase with the voltage in Figure 32c, which indicates active power injection. On the other hand, in Figure 32d the phase displacement of voltage

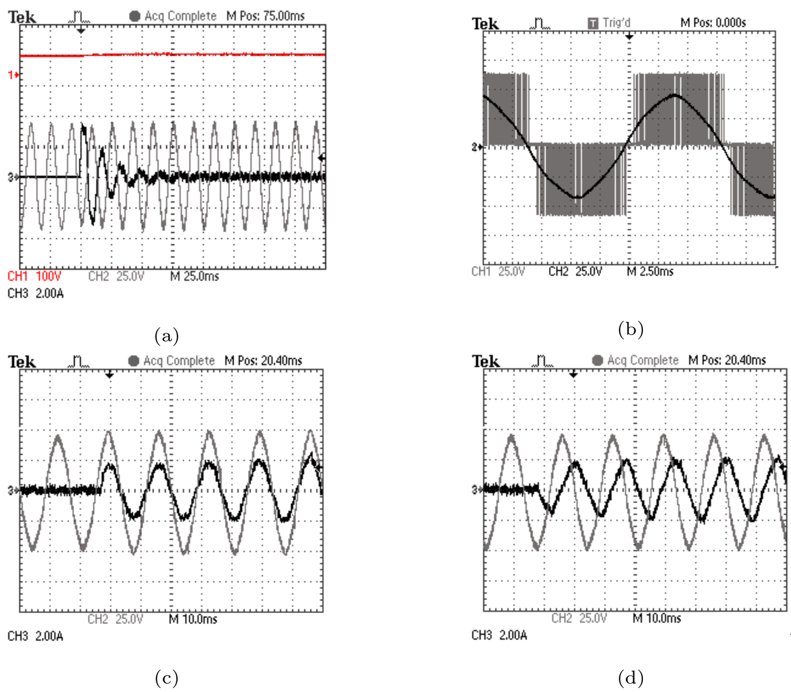

Figure 32: Experimental results of the grid current control: (a) Transient during the connection to the grid; (b) Steady-stage grid voltage and inverter output voltage v_s; (c) Transient response during an active power step; (d) Transient response during a reactive power step.

and current is 90 degrees, which means reactive power injection.

7. Ancillary services: Reactive power control

As previously mentioned, reactive power control and harmonic current compensation are ancillary functions which are expected to be included in the next generation of PV inverters. These additional functions require improvements in the traditional control approach which are highlighted in Figure 33. As observed, the following blocks are added: reactive power reference selection, harmonic detection, dynamic saturation, and harmonic control. This section focuses on the reactive power control. The next section discusses the harmonic current compensation.

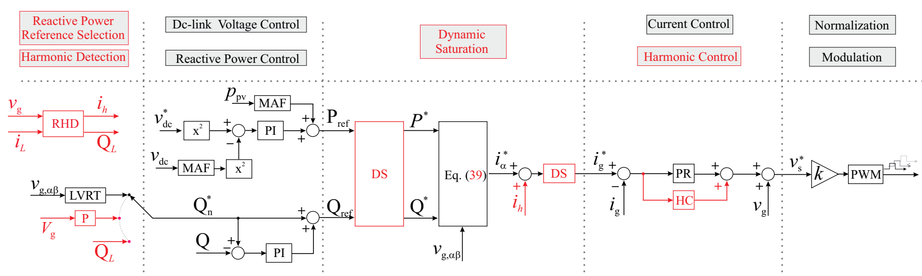

Figure 33: Example of a possible control strategy for the next-generation of single-phase PV inverters. The highlighted blocks represent the additional structures in comparison with state-of-art PV inverters.

7.1. Reactive power control modes

In the next generation of PV inverters, a flexible reactive power control is expected. The first control mode is the LVRT strategy, which was described in section 6.2. It is important to remark this strategy is already required by the standards.

The second control mode is called voltage support mode. When a high penetration of PV systems is considered, during periods of high irradiance, the voltage in the distribution systems can increase, as illustrated in Figure 34. Under such conditions, due to the limited capability of the voltage regulators, the grid voltage increases, and some PV systems may disconnect due to overvoltage

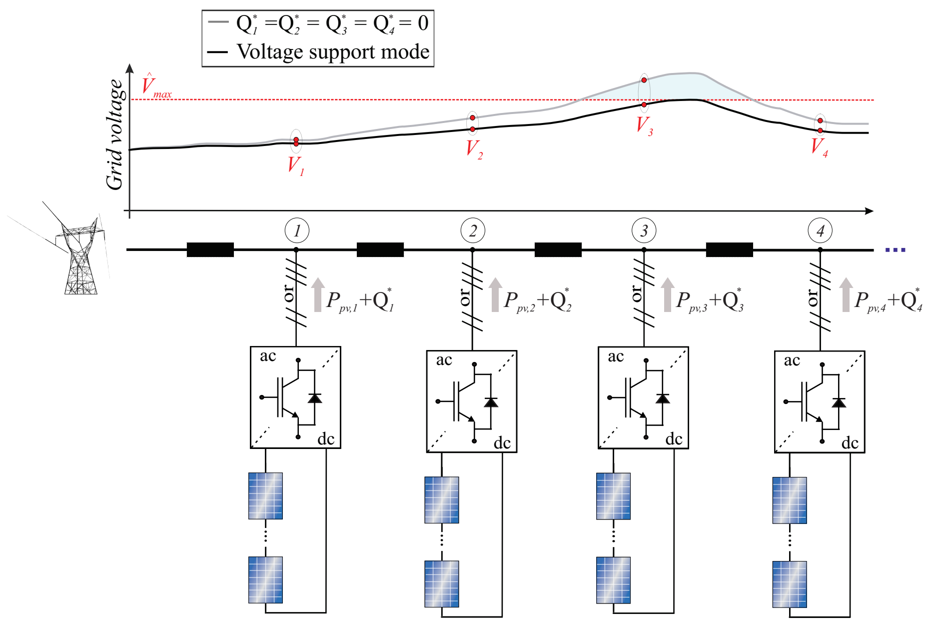

Figure 34: Effect of the voltage support mode in the PCC voltage of a distribution system with high penetration of PV systems.

in the extreme case. Therefore, the distribution system characteristics pose challenges to the increasing insertion of PV systems.

The voltage support mode consists in compute a reactive power reference which is exchanged with the grid when the voltage is outside predefined limits. This extra reactive power injection can limit the increase of the grid voltage, as shown in Figure 34. Therefore, the voltage support mode is an ancillary service which can contribute to increase the number of PV systems installed in a distribution system.

The third reactive power control mode is the reactive power compensation of local loads. The objective of this strategy is to obtain a unitary power factor in the point of common coupling (PCC). This approach is remarkably interesting when industrial systems are taken into account. Indeed, industries draw a certain amount of active and reactive power from the grid to supply the power demanded by its load. However, the introduction of a photovoltaic plant reduces the liquid active power demand from the grid due to local generation, as illustrated in Figure 35. According to the power triangle, reduction of active power leads to a reduction in the power factor. The industry power factor must be corrected according to the standards, otherwise there will be extra fees over the exceeding reactive power. Under such conditions, this reactive power control mode can avoid paying fees due to low PF. This approach is investigated in details by [35].

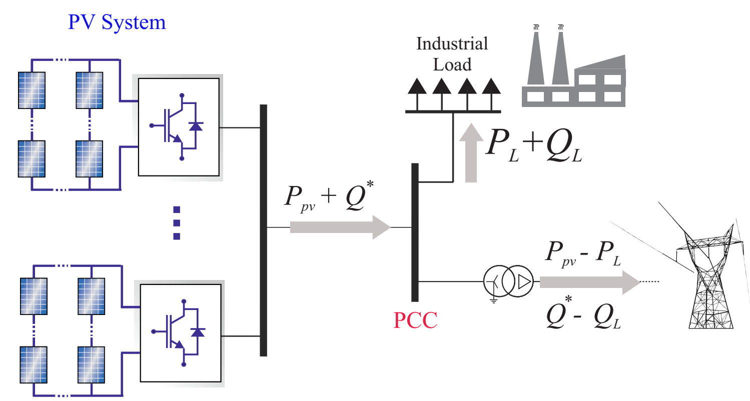

Figure 35: Example of a grid-connected PV system in an industrial plant. As observed, when the PV inverter injects the load reactive power, the power factor at the PCC is unitary.

7.2. Dynamic saturation scheme

Independent of the control mode employed, a dynamic saturation is required to guarantee that the PV inverter current does not exceed the rated value during ancillary services. Neglecting the grid voltage harmonics, the active and reactive power are driven by the fundamental current. Therefore, the dynamic saturation can be performed in the active and reactive power reference P_{ref} and Q_{ref}, as shown in Figure 33. Accordingly,

$$\sqrt{P_{\text{ref}}^2 + Q_{\text{ref}}^2} \leq S_{\text{r}} = \frac{V_{\text{g}} \widehat{I}_{\text{r}}}{\sqrt{2}}, \tag{65}$$

where S_{r} is the rated apparent power, V_{g} is the line-to-line rms value of grid voltage and $\widehat{I}_{\text{r}}$ is the inverter rated current.

The dynamic saturation equations are obtained based on the defined priority. If the reactive power has priority over the active power injection, the dynamic saturation is defined as:

$$\begin{cases} Q^{*} = Q_{\mathrm{ref}}, \quad if \quad |Q_{\mathrm{ref}}| \leq S_{\mathrm{r}}, \\ Q^{*} = S_{\mathrm{r}}, \quad if \quad |Q_{\mathrm{ref}}| > S_{\mathrm{r}}, \\ P^{*} = min\left(\sqrt{S_{\mathrm{r}}^{2} - {Q_{\mathrm{ref}}}^{2}}, P_{\mathrm{ref}}\right), \quad if \quad |Q_{\mathrm{ref}}| \leq S_{\mathrm{r}}, \\ P^{*} = 0, \quad if \quad |Q_{\mathrm{ref}}| > S_{\mathrm{r}}. \end{cases} \tag{66}$$

On the other hand, when the active power has priority over the reactive power injection, the dynamic saturation is defined as:

$$\begin{cases} P^{*} = P_{\mathrm{ref}}, \quad if \quad P_{\mathrm{ref}} \leq S_{\mathrm{r}}, \\ P^{*} = S_{\mathrm{r}}, \quad if \quad P_{\mathrm{ref}} > S_{\mathrm{r}}, \\ Q^{*} = min\left(\sqrt{S_{\mathrm{r}}^{2} - {P_{\mathrm{ref}}}^{2}}, Q_{\mathrm{ref}}\right), \quad if \quad P_{\mathrm{ref}} \leq S_{\mathrm{r}}, \\ Q^{*} = 0, \quad if \quad P_{\mathrm{ref}} > S_{\mathrm{r}}. \end{cases} \tag{67}$$

It is important to remark that anti-windup strategies must be included in the dc-link voltage and reactive power compensators to improve the dynamic performance, as suggested in [5].

The performance of the reactive power dynamic saturation scheme is evaluated through simulation. The parameters of Tables 3, 4, 5, and 6 are employed. Initially, $G = 500$ W/m^2 and $T = 35.63$ °C. A constant reactive power reference $Q_{\mathrm{n}}^{*} = 1500$ var is assumed. At time 3 seconds, the irradiance increases in ramp (2000 W/(m^{2}s)) to $G = 1000$ W/m^2. At time t = 3.5 seconds, the irradiance reduces to $G = 500$ W/m^2. The priority of the active power injection is assumed. Therefore, equation (67) is employed in the dynamic saturation algorithm.

Figure 36a presents the active power injected into the grid. As observed, the active power profile follows the behavior of the solar irradiance profile. The dc-link voltage is presented in Figure 36b. No significant transient is observed, which shows the robustness of the dc-link voltage control. The second-harmonic ripple increases because the converter is processing more apparent power, as predicted by equation (32).

The reactive power injected into the grid is presented in Figure 36c. Before t = 3 seconds, the inverter injects the reactive power reference ($Q_{\mathrm{n}}^{*} = 1500$ var). When the irradiance increases, the dynamic saturation reduces the injected reactive power to do not exceed the inverter rated current. When the irradiance reduces (after 3.5 seconds), the injected reactive power reaches the reference value again. The grid current is shown in Figure 36d. As noticed, the dynamic saturation scheme guarantees that the inverter current is below its rated current (15 A).

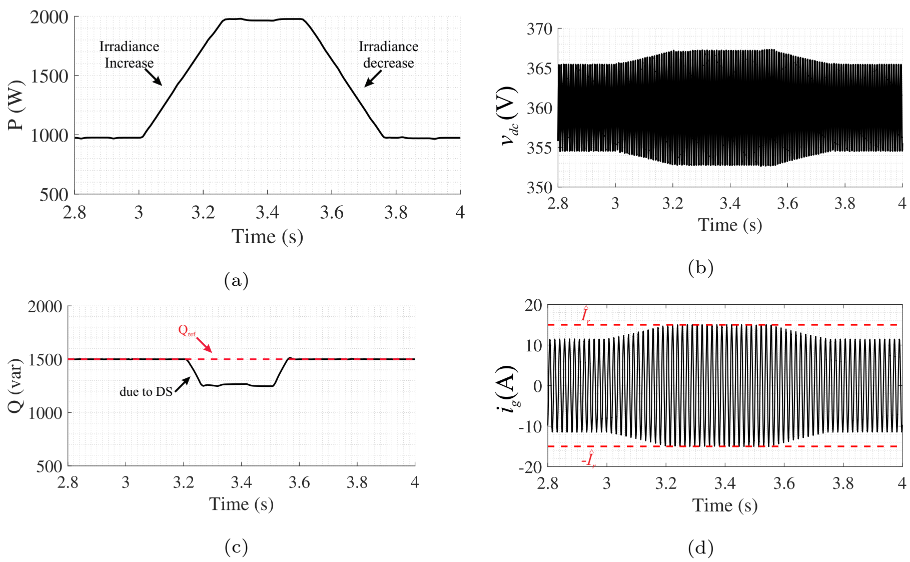

Figure 36: Simulation results of dynamic current saturation scheme: (a) Active power injected into the grid; (b) Dc-link voltage; (c) Reactive power injected into the grid; (d) Grid current.

8. Ancillary services: Harmonic Current Compensation

The harmonic current compensation requires three main structures: harmonic detection, harmonic controller, and dynamic saturation algorithm. The harmonic detection has been strongly investigated in literature. Usually, the harmonic detection can be implemented in frequency domain or in time domain. The frequency domain harmonic detection is usually based on Fourier or Wavelet transform [36]. These approaches usually lead to a selective harmonic detection, i.e., only the components of interest are detected.

Time domain harmonic detection methods can be divided into adaptive filtering or power theory-based approaches. The adaptive filtering methods lead to a selective harmonic detection. Different bandpass and/or notch filter structures are employed to detect the individual harmonics. Therefore, this approach is interesting for selective harmonic compensation. On the other hand, power theory-based approaches usually compute the total harmonic current of the load [37]. Therefore, these algorithms do not obtain the individual harmonic components [10].

The second structure required by harmonic current compensation is the harmonic controller. Different approaches have been proposed in literature. The most popular are the proportional multi-resonant (PMR) controllers and the repetitive controllers [6]. Other references present non-linear controllers for harmonic compensation. Examples are the hysteresis controller, sliding mode controller, passivity-based controller, dead-beat controller, neural networks and fuzzy logic [6, 38].

As observed, the first two structures have been strongly studied in literature. However, few works discuss the harmonic current dynamic saturation. Indeed, the PV inverter presents a rated current $\widehat{I}_{\mathrm{r}}$. When the current waveform peak is higher than the inverter rated current, some saturation strategy must be employed. Because the solar irradiance is not constant during the day, the margin for harmonic compensation changes. Therefore, algorithms are required to guarantee that the inverter operate beyond its rated current.

Figure 37 illustrates the dynamic saturation concept. The reference currents shown in Figure 37a are supposed. These currents are in per unit values, where the inverter rated current $\widehat{I}_{\mathrm{r}}$ is 1 pu. As observed, the reference i_{α}^{*} computed by the outer loops is a sinusoidal waveform. On the other hand, the detected

[10] It is important to remark that the harmonic detection must be implemented in the inverter controller, which means that methods with reduced computational burden are preferred.

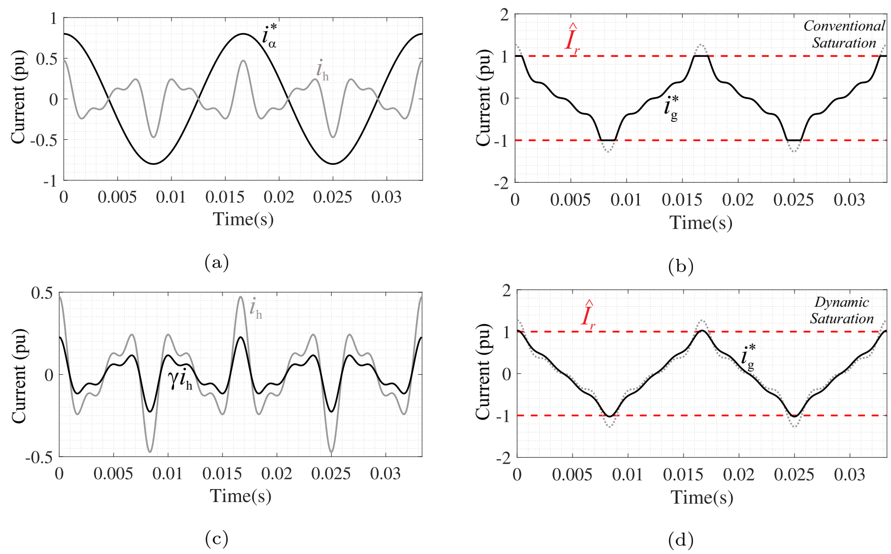

Figure 37: Illustration of the dynamic saturation concept: (a) Fundamental current reference and the detected harmonic component; (b) Inverter current reference for the traditional saturation scheme; (c) Effect of the harmonic compensation factor in the inverter harmonic current; (d) Inverter current reference for the dynamic saturation scheme.

harmonic current i_h is assumed to be given by:

$$i_\mathrm{h} = \sum_{k=2}^{m} I_\mathrm{k} cos\left(k\omega_\mathrm{n}t + \varphi_\mathrm{h}\right) \tag{68}$$

where m is the maximum harmonic order to be compensated.

The traditional concept of current saturation is presented in Figure 37b. As observed, when the instantaneous value of the current reference is higher than the rated value, its value is limited. Although this strategy is quite simple to be implemented, it leads to the injection of undesirable harmonics in the grid. The saturation happens when the instantaneous value of inverter current reference $i^*_\mathrm{g} = i^*_\alpha + i_\mathrm{h}$ is higher than the rated value $\widehat{I_\mathrm{r}}$.

An alternative way to solve the problem is to modify the inverter current reference computation as follows:

$$i^*_\mathrm{g} = i^*_\alpha + \gamma i_\mathrm{h} \tag{69}$$

where $0 \leq \gamma \leq 1$. This factor is referred in this chapter as *harmonic compensation factor*.

The harmonic compensation factor reduces the harmonic current amplitude to fulfill the following inequality:

$$|i_{\mathrm{g}}^{*}| \leq \widehat{I}_{\mathrm{r}}. \tag{70}$$

Figure 37c illustrates the effect of the harmonic compensation factor γ. This factor guarantees a partial compensation of the harmonic content and it does not prioritize any harmonic frequency. The inverter reference current with the dynamic saturation scheme is presented in Figure 37d. In this situation, the low frequency content of the harmonic current is fully controlled.

The next subsections present two dynamic saturation schemes for PV inverters with ancillary services capability: the open loop dynamic saturation and the closed loop dynamic saturation schemes.

8.1. Open loop strategy

The open loop dynamic saturation strategy was firstly proposed by reference [39]. The block diagram of this scheme is presented in Figure 38. The outer loops compute the fundamental current reference i_{α}^{*}. The harmonic detection algorithm computes the harmonic current reference i_{h}. These variables are the inputs of the dynamic saturation algorithm which computes the harmonic compensation factor γ_0. A low-pass filter is included to attenuate the oscillations in γ is steady state, as discussed in [8].

The dynamic saturation algorithm is executed in the control sampling frequency. However, its output is updated only twice per fundamental cycle. This algorithm

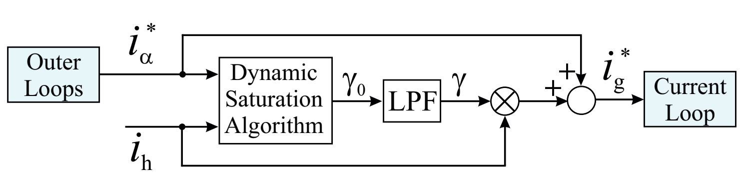

Figure 38: Block diagram of the open loop dynamic saturation strategy.

presents 3 steps:

1. Firstly, the peak value of $|i_{\mathrm{g}}^*| = |i_\alpha^* + i_{\mathrm{h}}|$ is computed by comparing the samples during half fundamental cycle. The instantaneous values of i_α^* and i_{h} which correspond to the peak value are stored. These values are denoted by I_α^* and I_{h};
2. Then, the trivial conditions are verified. If $I_\alpha^* + I_{\mathrm{h}} \leq \widehat{I}_{\mathrm{r}}$, $\gamma_0 = 1$ and full compensation is obtained. If $I_\alpha^* > \widehat{I}_{\mathrm{r}}$ or if $I_{\mathrm{h}} = 0$, $\gamma_0 = 0$ and the harmonic compensation is not performed;
3. If the conditions of step 2 are not fulfilled, partial harmonic compensation is performed. Under such conditions, the harmonic compensation factor is computed by:

$$\gamma_0 = \frac{\widehat{I}_{\mathrm{r}} - I_\alpha^*}{I_{\mathrm{h}}}. \tag{71}$$

8.2. Closed loop strategy

The first idea of a closed loop dynamic saturation strategy were initially presented in [40]. Recently, improvements in this approach and its dynamic modelling were presented by [8]. The block diagram of this scheme is shown in Figure 39a. As observed, the inverter reference current is computed based on equation (69). A peak detector algorithm is employed to obtain $I_{\mathrm{m}} = \max(|i_{\mathrm{g}}^*|)$. The absolute value of i_{g} guarantees the peak detection each half of the grid period. Then, a control loop based on a proportional integral controller computes γ.

The major issue of the closed loop scheme is the PI controller tuning. This task is challeging because the signals i_α^* and i_{h} are time variant. This challenge can be solved based on the simplified block diagram of Figure 39b. This block diagram assume that I_{m} can be roughly approximated using equation (71), as follows:

$$I_{\mathrm{m}} \approx I_\alpha^* + \gamma I_{\mathrm{h}}. \tag{72}$$

The transfer function $G_{\mathrm{pd}}(s)$ represents the delay caused by the peak detector algorithm, which can be represented by:

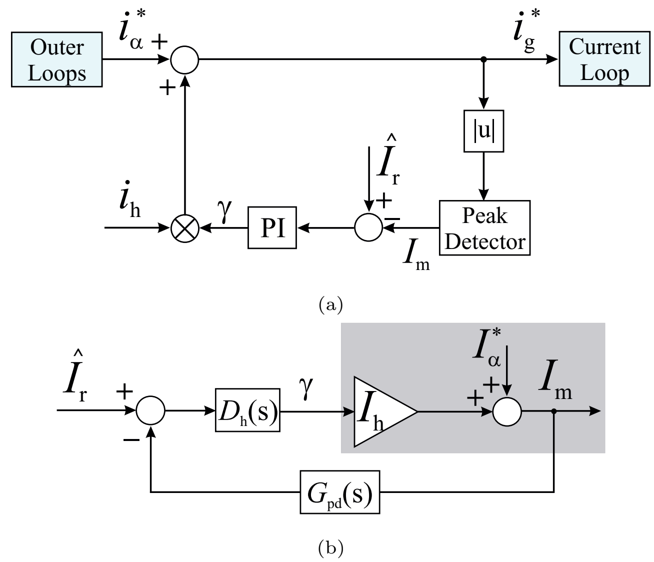

Figure 39: Closed loop dynamic saturation strategy: (a) Block diagram; (b) Simplified block diagram for control tuning.

$$G_{\mathrm{pd}}(s) = e^{-T_{\mathrm{pd}}s} \approx \frac{1}{T_{\mathrm{pd}}s + 1} \tag{73}$$

where $T_{\mathrm{pd}} = \frac{1}{2f_{\mathrm{n}}}$.

Neglecting the disturbance I_α^*, the open loop transfer function is given by:

$$\frac{\widehat{I}_{\mathrm{r}}(s)}{I_{\mathrm{m}}(s)} = \overbrace{k_{\mathrm{p,ds}}\frac{s + \frac{k_{\mathrm{i,ds}}}{k_{\mathrm{p,ds}}}}{s}}^{D_{\mathrm{h}}(s)} \frac{I_{\mathrm{L}}}{T_{\mathrm{pd}}s + 1}, \tag{74}$$

Under such conditions, the poles placement method leads to the following tuning formulas:

$$k_{\mathrm{p,ds}} = \frac{2\pi f_{\mathrm{c,ds}} T_{\mathrm{pd}}}{I_{\mathrm{L}}} \tag{75}$$

$$k_{\mathrm{i,ds}} = \frac{2\pi f_{\mathrm{c,ds}}}{I_{\mathrm{L}}} \tag{76}$$

where $f_{\mathrm{c,ds}}$ is the pole of the closed loop transfer function. This value must be selected lower than the grid frequency. It is important to remark that the output of the PI controller must be saturated between 0 and 1. Under such conditions, an anti-windup PI controller is employed.

8.3. Experimental results

This section presents some experimental results of the open loop and closed loop dynamic saturation algorithms. The parameters of the experimental setup are presented in Table 8. This setup presents an L filter and a dc-source is connected to the inverter dc-link. The control is implemented in a F28335 floating-point DSP from Texas Instruments. A single-phase diode rectifier is used as a nonlinear load. Its harmonic current is detected based on multiple bandpass filters tuned to each harmonic frequency, as proposed by [34].

Table 8: Parameters of experimental setup.

Parameters	Value
Grid voltage (line-to-line RMS) V_{g}	127 V
Switching frequency f_{sw}	9,000 Hz
Sampling frequency f_{s}	9,000 Hz
Dc-link voltage reference v_{dc}^{*}	370 V
L filter inductance L_{f}	4 mH
Inductor ESR R_{L}	40 mΩ
Rated current $\widehat{I}_{\mathrm{r}}$	18 A

A PMR controller with resonance frequencies at fundamental and seven tuned at the odd harmonics until the 15th harmonic order is implemented. The Tustin with pre-warping discretization method was employed. The dynamic saturation algorithms are designed as discussed in [8]. For the open loop scheme, the bandpass filter cut-off frequency is selected 15 Hz. For the closed loop scheme, the closed loop pole frequency is selected to be 4 Hz (3 decades below the delay of the peak detector algorithm).

At t = 0, the fundamental current reference is set to zero. Then, at t = 1.2 seconds, the fundamental active current reference is increased to 6 A. Finally, at t = 2.4 seconds, the fundamental active current reference is increased to 12 A. Figure 40a presents the dynamics of the harmonic compensation factor for both dynamic saturation schemes. As noted, initially the harmonic compensation factor is 1, which indicates the full compensation of the load current. When the fundamental current increases, the harmonic compensation factor reduces to guarantee that the inverter output current is beyond the rated values. In addition, the open loop and closed loop schemes present similar transient response and same steady-state value. Because of this fact, the next results focus on the open loop scheme.

Figure 40b shows the steady-state waveforms at t = 0.5 seconds for load current, inverter output current and grid current for the open-loop scheme. As observed, the PV inverter synthesize a distorted current to provide the total harmonic compensation. In addition, its maximum value is lower than the rated current $\widehat{I}_{\mathrm{r}}$. Because the total harmonic compensation is reached, the grid current is approximately sinusoidal.

At time t = 1.2 and t = 2.4 seconds, a step is applied in the fundamental current. As observed, the harmonic compensation factor reduces to 0.9 and 0.42, respectively. Under such conditions, the PV inverter performs the partial harmonic compensation of the load current. Figure 40c shows the steady-state waveforms at t = 2.5 seconds. As observed, the inverter current peak value is equal to the rated value $\widehat{I}_{\mathrm{r}}$. Because the compensation is partial, the grid current harmonic distortion becomes distorted.

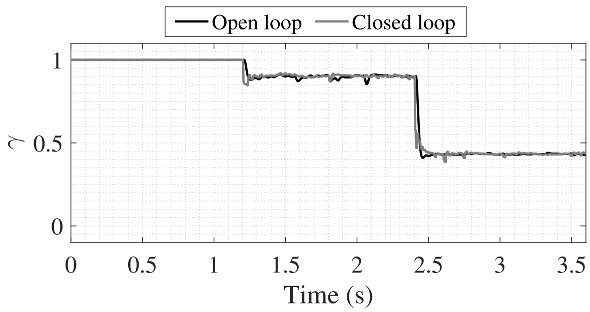

(a)

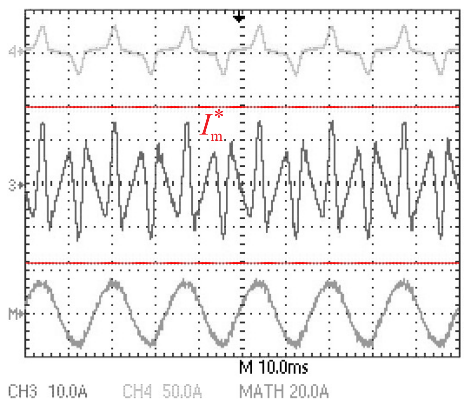

(b)

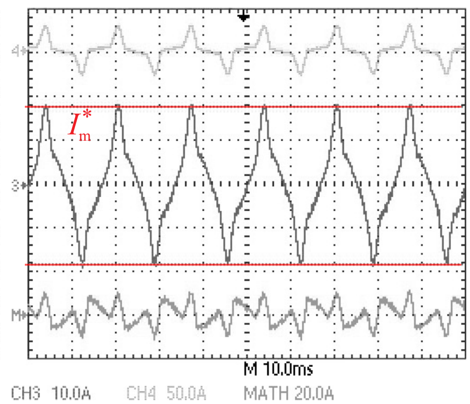

(c)

Figure 40: Experimental results for the dynamic saturation algorithms: (a) Harmonic compensation factor for both open loop and closed loop schemes; (b) Steady-state waveforms for the open loop scheme at t = 0.5 seconds; (c) Steady-state waveforms for the open loop scheme at t = 2.5 seconds. *Remark*: The experimental result of γ was obtained from recordings of the DSP memory. Ch3 is the is the inverter output current, CH4 is the load current and MATH is the grid current.

The transient performance is evaluated in Figure 41 at t = 2.4 seconds for the open loop scheme. As observed, the grid current exceeds the rated value only in the first fundamental cycle after the disturbance. The overshoot is around 16 %. As noted, both dynamic saturation schemes lead to suitable results for implementation in the next generation of PV inverters with harmonic compensation capability. Additional comparison of these methods can be found in [8]. In addition, the implementation of dynamic saturation schemes for three-phase inverters can be found in [5].

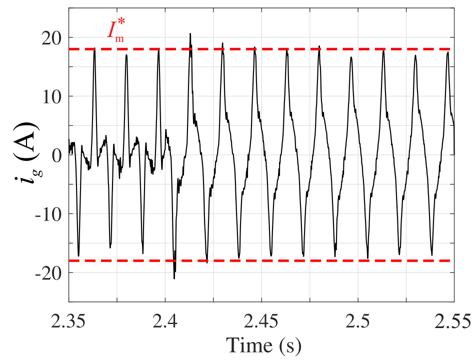

Figure 41: Transient performance at t = 2.4 seconds for the open loop dynamic saturation scheme. *Remark*: This experimental result was obtained from recordings of the DSP memory.

9. Conclusions and future trends

This chapter drives the readers into the main strategies implemented in a single-phase PV inverter. Besides, the connection between the modelling process, the control strategies and the grid code requirements are explored, and the dependency between them is the key point in the integration of PV systems into the power system. Since PV systems have the possibility to be spread around the entire power system, they also can be used to contribute with the overall power quality. Nowadays, PV inverters can provide auxiliary services to attend the grid code, such as contributing with reactive power during voltage sag or over-voltage. However, other goals can be implemented in the PV inverter firmware, and the main trends are:

- Reactive power control to attend local loads, replacing shunt capacitor banks;
- Harmonic current injection, replacing active filters;
- Grid frequency support, when PV system are integrated with energy storage systems;

- PV inverters will become smart and strategic devices in the system, providing 24-7 services.

In this context of ancillary services, further issues arise:

- Who will pay for these services?
- How to measure the impact in the PV inverter lifetime?
- Will the silicon-based semiconductor devices replaced by low loss power devices, such as those based on silicon carbide (SiC)?
- How will be the communication exchange between the PV inverter and the grid operator?
- Will the PV systems integrated with energy storage systems be allowed to operate in island mode?

References

[1] M. Woodhouse, R. Jones-Albertus, D. Feldman, R. Fu, K. Horowitz, D. Chung, D. Jordan, S. Kurtz, On the path to sunshot: The role of advancements in solar photovoltaic efficiency, reliability, and costs, Technical Report NREL/TP-6A20-65872, National Renewable Energy Laboratory, 2016.

[2] M. Hussin, A. Omar, S. Shaari, N. M. Sin, Review of state-of-the-art: Inverter-to-array power ratio for thin – film sizing technique, Renewable and Sustainable Energy Reviews 74 (2017) 265 – 277.

[3] A. Sangwongwanich, Y. Yang, D. Sera, F. Blaabjerg, D. Zhou, On the impacts of pv array sizing on the inverter reliability and lifetime, IEEE Transactions on Industry Applications 54 (2018) 3656–3667.

[4] J. D. Mondol, Y. G. Yohanis, B. Norton, Optimal sizing of array and inverter for grid-connected photovoltaic systems, Solar Energy 80 (2006) 1517 – 1539.

[5] L. S. Xavier, A. F. Cupertino, H. A. Pereira, Ancillary services provided by photovoltaic inverters: Single and three phase control strategies, Computers & Electrical Engineering 70 (2018) 102 – 121.

[6] K. Zhou, D. Wang, Y. Yang, F. Blaabjerg, Periodic Control of Power Electronic Converters, 1st ed., IET Press, 2016.

[7] V. M. R. de Jesus, A. F. Cupertino, L. S. Xavier, H. A. Pereira, V. F. Mendes, Comparison of mppt strategies in three-phase photovoltaic inverters applied for harmonic compensation, IEEE Transactions on Industry Applications 55 (2019) 5141–5152.

[8] L. S. Xavier, A. F. Cupertino, H. A. Pereira, V. F. Mendes, Partial harmonic current compensation for multifunctional photovoltaic inverters, IEEE Transactions on Power Electronics 34 (2019) 11868–11879.

[9] A. McEvoy, L. Castaner, T. Markvart, Physics of Solar Cells: From Basic Principles to Advanced Concepts, 2nd ed., Elsevier, 2012.

[10] P. Würfel, U. Würfel, Physics of Solar Cells: From Basic Principles to Advanced Concepts, 3rd ed., John Wiley & Sons, 2016.

[11] Fraunhofer Institute, Photovoltaic report - 2019, 2020. URL: `https://www.ise.fraunhofer.de/content/dam/ise/de/documents/publications/studies/Photovoltaics-Report.pdf`.

[12] National Renewable Energy Laboratory, Best research-cell efficiency chart, 2020. URL: `https://www.nrel.gov/pv/cell-efficiency.html`.

[13] N. Barth, R. Jovanovic, S. Ahzi, M. A. Khaleel, Pv panel single and double diode models: Optimization of the parameters and temperature dependence, Solar Energy Materials and Solar Cells 148 (2016) 87 – 98. Solar Cells and Storage.

[14] P. Singh, S. Singh, M. Lal, M. Husain, Temperature dependence of i–v characteristics and performance parameters of silicon solar cell, Solar Energy Materials and Solar Cells 92 (2008) 1611 – 1616.

[15] D. Sera, R. Teodorescu, P. Rodriguez, Pv panel model based on datasheet values, in: 2007 IEEE International Symposium on Industrial Electronics, 2007, pp. 2392–2396.

[16] M. G. Villalva, J. R. Gazoli, E. R. Filho, Comprehensive approach to modeling and simulation of photovoltaic arrays, IEEE Transactions on Power Electronics 24 (2009) 1198–1208.

[17] M. G. Villalva, Modeling and simulation of photovoltaic arrays, 2020. URL: `https://sites.google.com/site/mvillalva/pvmodel`.

[18] D. T. Lobera, S. Valkealahti, Dynamic thermal model of solar pv systems under varying climatic conditions, Solar Energy 93 (2013) 183 – 194.

[19] M. N. H. Khan, M. Forouzesh, Y. P. Siwakoti, L. Li, T. Kerekes, F. Blaabjerg, Transformerless inverter topologies for single-phase photovoltaic systems: A comparative review, IEEE Journal of Emerging and Selected Topics in Power Electronics 8 (2020) 805–835.

[20] SMA Solar Technology AG, Module technology:sma inverters provide the optimum solution for every module, 2020. URL: `http://files.sma.de/dl/7418/Duennschicht-TI-UEN114630.pdf`.

[21] S. Lyden, M. Haque, Maximum power point tracking techniques for photovoltaic systems: A comprehensive review and comparative analysis, Renewable and Sustainable Energy Reviews 52 (2015) 1504 – 1518.

[22] A. Sangwongwanich, Y. Yang, D. Sera, H. Soltani, F. Blaabjerg, Analysis and modeling of interharmonics from grid-connected photovoltaic systems, IEEE Transactions on Power Electronics 33 (2018) 8353–8364.

[23] H. Schmidt, How fast does an mpp tracker really need to be?, in: 24th European Photovoltaic Solar Energy Conference, 2009, p. 3273 – 3276.

[24] W. Yao, Y. Yang, X. Zhang, F. Blaabjerg, P. C. Loh, Design and analysis of robust active damping for lcl filters using digital notch filters, IEEE Transactions on Power Electronics 32 (2017) 2360–2375.

[25] N. Hoffmann, F. W. Fuchs, M. P. Kazmierkowski, D. Schröder, Digital current control in a rotating reference frame - part i: System modeling and the discrete time-domain current controller with improved decoupling capabilities, IEEE Transactions on Power Electronics 31 (2016) 5290–5305.

[26] C. C. Gomes, A. F. Cupertino, H. A. Pereira, Damping techniques for grid-connected voltage source converters based on lcl filter: An overview, Renewable and Sustainable Energy Reviews 81 (2018) 116 – 135.

[27] A. G. Yepes, F. D. Freijedo, . Lopez, J. Doval-Gandoy, High-performance digital resonant controllers implemented with two integrators, IEEE Transactions on Power Electronics 26 (2011) 563–576.

[28] Y. Tang, C. Yoon, R. Zhu, F. Blaabjerg, Generalized stability regions of current control for lcl-filtered grid-connected converters without passive or active damping, in: 2015 IEEE Energy Conversion Congress and Exposition (ECCE), 2015, pp. 2040–2047.

[29] A. F. Cupertino, L. S. Xavier, E. M. Brito, V. F. Mendes, H. A. Pereira, Benchmarking of power control strategies for photovoltaic systems under unbalanced conditions, International Journal of Electrical Power & Energy Systems 106 (2019) 335 – 345.

[30] Y. Du, D. D.-C. Lu, Power System Harmonics - Analysis, Effects and Mitigation Solutions for Power Quality Improvement, IntechOpen, 2018, pp. 52–64.

[31] D. G. Holmes, T. A. Lipo, B. P. McGrath, W. Y. Kong, Optimized design of stationary frame three phase ac current regulators, IEEE Transactions on Power Electronics 24 (2009) 2417–2426.

[32] H. A. Pereira, R. M. Domingos, L. S. Xavier, A. F. Cupertino, V. F. Mendes, J. O. S. Paulino, Adaptive saturation for a multifunctional three-phase photovoltaic inverter, in: 2015 17th European Conference on

Power Electronics and Applications (EPE'15 ECCE-Europe), 2015, pp. 1–10.

[33] P. R. Remus Teodorescu, Marco Liserre, Grid Converters for Photovoltaic and Wind Power Systems, 1st ed., Wiley-IEEE Press, 2011.

[34] L. S. Xavier, A. F. Cupertino, J. T. de Resende, V. F. Mendes, H. A. Pereira, Adaptive current control strategy for harmonic compensation in single-phase solar inverters, Electric Power Systems Research 142 (2017) 84 – 95.

[35] L. Gusman, H. Pereira, J. Callegari, A. Cupertino, Design for reliability of multifunctional pv inverters used in industrial power factor regulation, International Journal of Electrical Power & Energy Systems 119 (2020) 105932.

[36] L. Asiminoaei, F. Blaabjerg, S. Hansen, Evaluation of harmonic detection methods for active power filter applications, in: Twentieth Annual IEEE Applied Power Electronics Conference and Exposition, 2005. APEC 2005., volume 1, 2005, pp. 635–641 Vol. 1.

[37] M. Godoy Simões, F. Harirchi, M. Babakmehr, Survey on time-domain power theories and their applications for renewable energy integration in smart-grids, IET Smart Grid 2 (2019) 491–503.

[38] R. Zahira, A. Peer Fathima , A technical survey on control strategies of active filter for harmonic suppression, Procedia Engineering 30 (2012) 686 – 693. International Conference on Communication Technology and System Design 2011.

[39] L. S. Xavier, V. M. R. de Jesus, A. F. Cupertino, V. F. Mendes, H. A. Pereira, Novel adaptive saturation scheme for photovoltaic inverters with ancillary service capability, in: 2017 IEEE 8th International Symposium on Power Electronics for Distributed Generation Systems (PEDG), 2017, pp. 1–8.

[40] Ting Qian, B. Lehman, G. Escobar, H. Ginn, M. Molen, Adaptive saturation scheme to limit the capacity of a shunt active power filter, in: Proceedings of 2005 IEEE Conference on Control Applications, 2005. CCA 2005., 2005, pp. 1674–1679.